

Laser-matter interactions, phase changes and diffusion phenomena
during laser annealing of plasmonic AlN:Ag templates and their
applications in optical encoding

A. Siozios¹, D.C. Koutsogeorgis², E. Lidorikis¹, G.P. Dimitrakopoulos³, N. Pliatsikas³, G.
Vourlias³, T. Kehagias³, P. Komninou³, W. Cranton^{2,4}, C. Kosmidis⁵, and P. Patsalas^{1,3,*}

¹*University of Ioannina, Department of Materials Science and Engineering, GR-45110 Ioannina,
Greece*

²*Nottingham Trent University, School of Science and Technology, NG11 8NS, Nottingham, UK*

³*Aristotle University of Thessaloniki, Department of Physics, GR-54124 Thessaloniki, Greece*

⁴*Sheffield Hallam University, Materials and Engineering Research Institute, Sheffield, S1 1WB,
UK*

⁵*University of Ioannina, Department of Physics, GR-45110 Ioannina, Greece*

**ppats@physics.auth.gr*

ABSTRACT.

Nanocomposite thin films incorporating silver nanoparticles are emerging as photosensitive templates for optical encoding applications. However, a deep understanding of the fundamental physicochemical mechanisms occurring during laser-matter interactions is still lacking. In this work, the photosensitivity of AlN:Ag plasmonic nanocomposites is thoroughly examined and a series of UV laser annealing parameters, such as wavelength, fluence and the number of pulses are investigated. We report and study effects such as the selective crystallization of the AlN matrix, the enlargement of the Ag nanoparticle inclusions by diffusion of laser-heated Ag and the outdiffusion of Ag to the film's surface. Detailed optical calculations contribute to the identification and understanding of the aforementioned physical mechanisms and of their dependency on the laser processing parameters. We are then able to predetermine the plasmonic response of processed AlN:Ag nanocomposites and demonstrate its potential by means of optically encoding an overt or covert cryptographic pattern.

KEYWORDS.

1. Surface Plasmon Resonance; 2. Laser Annealing; 3. Optical Encoding; 4. Nanocomposite Films; 5. Plasmonic Nanoparticles.

1. Introduction

The interaction of low intensity light with non-percolating metal nanoparticles (NP) inside a dielectric host is dictated by the Localized Surface Plasmon Resonance (LSPR), a collective oscillation of the metal's conduction electrons manifesting within a narrow spectral band around a resonance frequency.¹ The LSPR traits are strong light absorption, scattering and light field focusing on the NP surface, and are the keystone of the emerging field of plasmonics²⁻¹² which promises radical breakthroughs in optical storage and transport of information. Strong intensity laser light, on the other hand, interacts with the metal NPs in many more complex ways, which include the self assembly of particles from individual metal atoms,¹³ particle reshaping,¹⁴⁻²⁰ melting and recrystallization,²¹⁻²⁵ metal growth,²⁶ and even structural alteration of the dielectric matrix.²⁷ This photosensitivity is a property of the composite metallodielectric system and depends on the fine details of both the initial NP/host structure and the laser source. Laser processing thus emerges as a novel plasmonic formation tool, offering exceptional flexibility in controlling the shape, size and environment of plasmonic NPs, and thus their optical response. As a consequence, this type of processing is now being intensively investigated as a promising route for optical storage of information.^{21, 27-34}

We have recently demonstrated²⁷ that an intense single pulse of a UV laser (ArF, 193 nm) drastically alters the structure of plasmonic AlN:Ag templates at the nanoscale, causing Ag NP enlargement and reshaping within a concurrently recrystallized AlN matrix. These structural changes render a strong reflectance contrast between treated and untreated regions, and as a result, a color-sensitive optical encoding scheme was proposed.²⁷ However, the fundamental mechanisms and fine-tune process details dictating the involved laser-matter interactions are not yet fully understood, limiting our ability for structure optimization and design. In this work, we

develop plasmonic AlN:Ag templates by sectored-target pulsed laser deposition (PLD)^{27,35,36} and we performed an extensive, thorough and in depth investigation of the laser-matter interactions, considering the laser wavelength (193 and 248 nm), fluence (200-600 mJ/cm²) and number of pulses, in terms of microstructure, surface chemistry and optical properties, characterized by scanning and transmission electron microscopy (SEM/TEM), X-ray photoelectron spectroscopy and X-ray-excited Auger electron spectroscopy (XPS/XAES) and optical reflectance spectroscopy. The experimental results are complemented by detailed Finite Difference Time Domain calculations targeted to identify and quantify the fundamental light-matter interactions and to obtain insights on the basic mechanisms of morphology change and on the design of selective absorption at specific template sites. We finally use the latter to demonstrate an AlN:Ag-based optical encoding technology that can provide selective overt or full-band (i.e. full visible range) covert patterns.

The paper is organized as follows: in section 2 we present the details of the experimental and computational methods used in this work, in section 3 we analyze the effects on the laser processing of the: (a) absence of Ag NPs from the film, (b) laser wavelength, (c) number of laser pulses, and (d) laser fluence. In section 4 we present the application of our process to optical encoding and in section 5 we conclude. In the online supplementary data, further details of the numerical calculations and durability tests of the encoded patterns in various chemical environments are shown.

2. Experimental and Computational Methods

The 70-100 nm thick AlN:Ag nanocomposite films were grown on two types of commercial substrates: *i.* Czochralski-grown *n*-type c-Si(100) prime wafers of 1-10 Ωcm resistivity, and *ii.*

c-cut (0001) double-side polished sapphire (Al_2O_3) wafers. Growth was done by Pulsed Laser Deposition (PLD) in an in-house-built high-vacuum system ($P_b < 5 \times 10^{-8}$ mbar) using the third harmonic of a Nd:YAG laser (LAMBDA-PHYSIK; 6 ns pulse duration, fluence 30 J/cm^2 and 10 Hz repetition rate) and rotating sample and target holders.^{27,35,36} The substrates were first cleaned in ultrasonic baths of tetra-chloro-ethylene, acetone and methanol, rinsed by de-ionized water and dried by dry N_2 gas shower. Then, they were chemically etched with HF prior to deposition. The substrates were placed 30 mm away from the PLD target. A thin ($< 3 \text{ nm}$) bond and cap layer of pure Al was first grown by PLD directly on the substrate. This layer was then transformed to AlN by *in-situ* exposure to Nitrogen plasma for 2 min.²⁷ The target for the PLD growth of AlN:Ag was a sectored one (standard KURT J. LESKER 2"×1/4" cylindrical Al sputter target, 99.99%, with Ag sectors, KURT J. LESKER 0.5 mm thick Ag foil, 99.99%, attached on the Al target and covering 25% of its area). PLD took place in a flowing N_2 ambient (N_2 purity=99.999%, $P_{\text{N}_2}=8 \times 10^{-2}$ mbar, N_2 flow was 50 sccm controlled by an electronic mass flow controller system). The partial cracking of N_2 was achieved by applying a -50 V *dc* bias to the sample during growth.

The laser annealing apparatus comprises of a light source (20 ns duration, unpolarized ArF or KrF laser), a variable attenuator for controlling the laser power, a beam homogenizer (EXITECH Ltd., type EX-HS-700D, providing 80% throughput and uniformity better than 2% throughout the square laser spot), a field lens, stainless steel mask stage for pattern creation, a projection lens ($\times 5$ or $\times 7$), the thin film sample and a X-Y translation stage by NEWPORT. The attenuator and projection lens conditions have been selected such as to provide the desired laser fluence on the samples surface, for the 193 nm and 248 nm laser beams. The laser patterns into AlN:Ag were either $3 \times 3 \text{ mm}^2$ squares (for using them for spectroscopic and structural analysis) or

micron-scale bits and stripes for encoding information; in the later case appropriate masks and the X-Y stage were used.

The optical properties of the samples have been studied by spectroscopic reflectance and transmittance measurements at normal incidence (250-780 nm spectral range) using a white light deuterium-halogen source, a co-axial fiber-optic assembly, a high line density grating and a CCD detector (AVANTES); the reflectivity spectra were normalized using two reference mirrors made of silver and gold.

TEM studies were performed using a 200 kV JEOL 2011 microscope (spherical aberration coefficient $C_s=0.5$ mm, point-to-point resolution 0.19 nm). Specimens for conventional TEM and high-resolution (HRTEM) observations, in plan-view and cross-section geometry, were prepared by mechanical thinning followed by Ar^+ ion milling. Identification of crystalline phases at the nanoscale has been accomplished by studying the spatial frequencies obtained after fast Fourier transform (FFT) of the HRTEM images. Secondary electron images (SEI) were recorded in a JEOL-JSM5260 scanning electron microscope (SEM) using a W-filament.

X-ray Photoelectron Spectroscopy (XPS), imaging XPS experiments and X-ray-excited Auger Electron Spectroscopy (XAES) observations and spectra were acquired in an Axis Ultra DLD system by KRATOS. A monochromated Al- K_{α} X-ray beam was used as the excitation sources for XPS and XAES. The pass energy was 160 eV for the XPS imaging experiments and 20 eV for the spectroscopic XPS/XAES experiments, respectively.

The spatially resolved optical absorption of the considered nanocomposite AlN:Ag films were studied by Finite Difference Time Domain (FDTD) calculations of representative model systems. FDTD solves the exact 3D full-vector Maxwell's equations on a computational grid.³⁷ For the

dispersive bulk Ag and Si index we perform Drude-Lorentz fits to the experimental complex dielectric functions³⁸ and the corresponding polarizability equations are solved in lock-step with Maxwell's equations³⁹ To account for small Ag nanoparticles we adjust the free-electron relaxation time τ according to $\tau^{-1} = \tau_{bulk}^{-1} + v_F / r$, where v_F is the Fermi velocity and r the nanoparticle radius.⁴⁰ The refractive index for the AlN matrix in the presence of the Ag nanoparticles is indirectly obtained from spectroscopic ellipsometry measurements of the as-grown samples, by performing a Maxwell-Garnett effective medium fit (see Fig. S1).

3. Results and Discussion

3.1 The effect of number of laser pulses

Previous works²⁷ have shown that the outdiffusion of Ag to the AlN:Ag surface during single-pulse laser annealing is substantially reduced compared to thermal annealing⁴¹. However, the potential gradual outdiffusion of Ag, when successive laser pulses are implemented, was not studied so far. Therefore, as a starting point in our research we consider the effect of the number of pulses used for laser annealing, which may be a crucial parameter that can affect the Ag diffusion processes and can be used to control the plasmonic response of the AlN:Ag templates. In order to investigate this, we considered the optical response of processed AlN:Ag by spectral reflectivity measurements and optical microscopy observations, and we evaluated the Ag outdiffusion by surface-sensitive XPS and XAES measurements. In particular, we processed an AlN:Ag template by the following laser annealing conditions: 1, 2 and 5 pulses at 193 nm and two different fluences (200 mJ/cm² and 400 mJ/cm², *i.e.* just above the annealing threshold and just below the ablation threshold) and 1, 2 and 5 pulses at 248 nm and 400 mJ/cm² (*i.e.* the fluence providing the best plasmonic response for this processing wavelength, as we will show

later). Note that the pulse repetition rate is below 1 Hz, which eliminates any possibility for transient thermal phenomena, and thus each successive pulse interacts with a perfectly relaxed AlN:Ag film at room temperature.

The optical reflectivity spectra after various numbers of pulses are presented in Fig. 1. In the case of the 193 nm wavelength and at low fluence (200 mJ/cm^2) (Fig. 1a) each successive pulse leads to a cumulative LSPR enhancement, in terms of the integral strength of the LSPR band indicating that the cumulative Ag diffusion results in shape and size improvement of the plasmonic nanoparticles; the Si substrate's E_1 critical point⁴² is also gradually emerging with the number of pulses due to the film's transparency, possibly because of the crystallization of AlN and the partial outdiffusion of Ag as we will discuss in more detail in the following paragraphs. On the contrary, for laser annealing at 193 nm and high fluence (400 mJ/cm^2) (Fig. 1b), the evolution of the reflectivity spectra with the number of laser pulses exhibits severe changes. The effect of one pulse at 400 mJ/cm^2 to the plasmonic response of the AlN:Ag system is more pronounced compared to that of 5 pulses at 200 mJ/cm^2 ; this indicates that the structural modifications taking place during the 193 nm laser annealing process are better associated with the laser fluence than with the total laser energy delivered. We will come back to this in the next section where we discuss the effect of laser fluence. For two pulses the LSPR band is substantially broader indicating an exceptionally broad size distribution of Ag nanoparticles that can only be explained by Ag outdiffusion. Finally, for 5 pulses the reflectivity spectrum is characteristic of a homogeneous Ag layer on top of the AlN:Ag film indicating that none of the remaining Ag has the form of nanoparticles.

In the case of laser annealing of AlN:Ag, using the 248 nm wavelength and fluence of 400 mJ/cm^2 , the picture is quite more complex. At the first laser pulse (Fig. 1c, circles), the pre-

existing LSPR band (Fig. 1, diamonds) is eliminated, possibly by dissolving of overheated, unstable Ag nanoparticles, whose constituent Ag atoms do not have the required diffusion time to reform into bigger Ag particles. The latter is, however, observed after the second pulse resulting in intense LSPR (Fig. 1c, up triangles). If we combine the low photon energy at 248 nm and the fact that the pulse duration is shorter than the time required for Ostwald ripening in a cold environment⁴³, and the fact that for the 248 nm wavelength the AlN environment is indeed relatively cold because the 248 nm beam is not absorbed by the AlN matrix due to its high fundamental gap (as we will also show later by detailed FDTD calculations), we may conjecture that the conditions are right for the Ostwald ripening process to take place in two steps: dissolution of particles for the first pulse and reforming of bigger particles close to the surface for the second pulse. Finally, the optical reflectivity spectrum for 5 pulses of 248 nm (Fig. 1c, down triangles) exhibits a broad LSPR band, resembling the broadening of the LSPR band for 193 nm at 2 pulses (Fig. 1b, up triangles), and blue-shifted compared to the band for two pulses of 248 nm. This indicates a surrounding medium that is less optically dense than AlN; a reasonable assumption to explain this could be that Ag has partially outdiffused and formed nanoparticles surrounded by air.

In order to quantify the gradual outdiffusion of Ag with the number of laser pulses, we acquired XAES spectra from the various regions of AlN:Ag surface treated by 1, 2, and 5 laser pulses using a 900 μm^2 acquisition area (for XAES raw data refer to online supplementary data). The Ag_{MNN} doublet is manifested for emitted Auger electrons' kinetic energies lying between 350 and 360 eV; this low kinetic energy renders an exceptionally short escape depth of four monolayers⁴⁴ for the Ag_{MNN} electrons. Consequently, XAES is the appropriate technique to investigate the outdiffusion of Ag with exceptional sensitivity, because the strength of the

measured Ag_{MNN} XAES signal is associated with the amount of Ag on the surface, for Ag coverage below six monolayers⁴⁵. Indeed, there is gradual increase of the peak to peak strength of the Ag_{MNN} XAES signal with the number of pulses at 193 nm and 248 nm and 400 mJ/cm² providing robust evidence of Ag outdiffusion during laser annealing of AlN:Ag (for XAES raw data refer to online supplementary data).

In order to compare quantitatively the Ag outdiffusion phenomena for the two wavelengths used for laser annealing, we report the relative strength of the derivative Ag_{MNN} XAES peak

$\left(\frac{dN/dE_{annealed}}{dN/dE_{as\ grown}}\right)$ vs. the number of pulses for the same fluence (400 mJ/cm²) in Fig. 2. For one and

two pulses there is a substantial increase of the Ag_{MNN} peak providing solid evidence for the gradual outdiffusion of Ag to the surface of AlN:Ag; the Ag outdiffusion is found to be more pronounced for the 248 nm wavelength, in agreement with FDTD calculations which indicated higher optical absorption and subsequently stronger overheating of the nanoparticles. For five laser pulses the relative strength of the Ag_{MNN} peak is reduced, possibly indicating the intense surface diffusion of Ag and Ostwald ripening of Ag islands⁴⁶. This effect is more pronounced for the 193 nm laser because of its higher photon energy.

3.2 The effect of laser wavelength

The produced AlN:Ag/Si samples consist of an amorphous AlN matrix with Ag inclusions of near spherical shape with an average size of ~3 nm following a very narrow size distribution, as it can be seen in Fig. 3a,b at different magnifications (for quantitative size distribution see Ref. 47). Exceptionally sharp AlN/Si interfaces, without any damage of the Si substrate can be seen in Fig. 3c. Selected area electron diffraction and HRTEM observations confirmed that the nanoparticles, depicted as darker regions in Fig. 3a,b, have the Ag crystal structure, i.e., there

was no intermixing between Ag and AlN. Measurements, using the Si substrate as reference, clearly verified the Ag {111} and {200} d -spacings. The untreated films give no trace of crystalline AlN; their density and refractive index of the AlN matrix have values inferior to crystalline w-AlN,⁴⁸ thus, confirming the amorphous nature of the matrix. The amorphous character of the AlN matrix is of paramount importance for practical applications, because its crystallization upon laser treatment may result in substantial spectral shift of the LSPR increasing the signal to noise ratio for optical encoding applications.²⁷

A major factor affecting the laser annealing process of is the laser wavelength, due to the different absorption coefficient values of the amorphous AlN matrix and the Ag NPs. We will study the annealing performance of two laser wavelengths, 193 and 248 nm. Cross section HRTEM images of the laser treated areas displayed in Fig. 3 reveal significant structural modifications for both wavelengths. In particular, laser annealing at 193 nm (Fig. 3d,e,f) leads to agglomeration of Ag nanoparticles and formation of larger nanoparticles close to the surface of the film. This enlargement of Ag nanoparticles can be described as an Ostwald ripening phenomenon, *i.e.* a thermodynamically-driven process whereby smaller nanoparticles are dissolved due to the instability resulting from the high surface-to-volume ratio, and the obtained atomic Ag is re-deposited on the surface of the more stable larger nanoparticles.

Another important feature of the 193 nm LA process is the structural modification of the AlN matrix material around the enlarged nanoparticles, and in particular, the partial crystallization of the AlN matrix into the wurtzite structure. w-AlN domains attached to Ag nanoparticles were observed by HRTEM in some regions of the samples (Fig. 3f), as verified by FFT analysis.²⁷ It is important to note that this structural change of AlN is observed only in the AlN:Ag nanocomposite films and not in pure PLD-grown AlN (for more details refer to online

supplementary data); therefore, the existence of Ag nanoparticles is essential for the crystallization of the matrix, and for the photosensitivity of the nanocomposite as a whole, not only due to their LSPR functionality, but also due to their physicochemical effects that will be described in the following in more detail based on FDTD calculations.

Similar results, but to a lesser extent, occur after the 248 nm laser treatment (Figs. 3g,h,i). This can be attributed to the lower delivered photon energy, which is below the AlN fundamental gap (6.2 eV), resulting in interaction solely with the Ag nanoparticles. As a result, the delivered energy to the substrate is higher than in the case of 193 nm LA, and thus the AlN/Si interface is significantly damaged. By the same token, the crystallization of the matrix is less likely to occur due to the lower effective temperature during laser annealing.

To get an insight into the light absorption dynamics inside the film during laser annealing, we performed FDTD simulations of a 60 nm thick nanostructured AlN:Ag film, where Ag consists of 3 nm diameter inclusions at 15% volume filling ratio randomly distributed inside the AlN matrix (extended details about the simulation formulation and as well as other simulated systems can be found in the online supplementary data). Laser light at 193 nm and/or 248 nm is normally incident on the AlN:Ag film. Part of it is reflected, part of it is absorbed inside the film, while the rest is absorbed by the Si substrate. The absorption percentage per nm of length for the two wavelengths is shown in Fig. 4a, where several configurations of randomly distributed Ag inclusions were averaged. We note that the difference between the two wavelengths with regard to the total film absorption is small, with the 193 nm illumination being slightly more absorbed. Evident in the figure is also the different standing wave patterns produced by the two wavelengths within the 60 nm film.

Of great importance is the distribution of absorbed light power among the different materials. This is shown in the histogram of Fig. 4b. Considering that the Ag nanoparticles are dispersed at only 15% by volume, it is apparent that they are the stronger absorbers in both cases. However, we find a significant difference between the two annealing wavelengths: for 193 nm, a much more balanced absorption between AlN and Ag occurs, with minimal light energy reaching the Si substrate. In contrast, for 248 nm, most of the absorption in the nanostructured film occurs within the Ag inclusions, while at the same time more light energy finds its way to the Si substrate causing significant damage. Color coded absorption distribution maps for these two cases are shown in Fig. 4c, for a slice of one of the different randomized configurations considered. The fact that Ag nanoparticles act as absorption centers explains why AlN crystallization occurs only within a few nanometers from the nanoparticles surface and not anywhere else. Furthermore, the more balanced absorption distribution in the film, as well as the minimal absorption by the Si substrate, qualitatively explains the superior annealing performance at 193 nm. On the other hand, for the 248 nm wavelength the AlN matrix remains at lower temperature and the Ag nanoparticles are overheated; as a result substantial diffusion of Ag is expected, which can explain the observed outdiffusion of Ag in the 248 nm case (XAES data of Fig. 2).

In Fig. 5 we plot the cumulative absorption in each different material as a function of Ag particle size for the two annealing wavelengths. Ordered Ag NP arrays are considered here only for simplicity. The superior performance of the 193 nm laser is apparent: stable performance for all particle sizes, more balanced absorption between matrix and inclusions, slightly stronger overall film absorption, smaller substrate absorption. The semi-open circles at 20 nm size correspond to the nanoparticles having a non-absorbing 2.5 nm crystalline AlN ($n=2.1$) shell around them.

They result into a small decrease in matrix absorption only, apparently the result of removing absorbing material and replacing with a non-absorbing one. The effect of shell creation thus is towards the direction of limiting the film's overall absorption, although it does not seem to be large enough to qualify as a self limiting factor for the annealing process.

The aforementioned structural modifications upon laser annealing greatly affect the plasmonic behavior of the AlN:Ag nanocomposites. Spectroscopic optical reflectance measurements (Fig. 6) reveal the main optical features. In particular, the reflectivity spectra of the as-grown film (black diamonds), the laser annealed film with one pulse of 193 nm at 400 mJ/cm² (purple triangles) and laser annealed film with two pulses of 248 nm at 400 mJ/cm² (magenta circles) are presented. The peak reflectivity for the non-annealed case is at ~410 nm and the peak for the annealed case is at ~470 nm [note that the reflectivity peak at ~365 nm is associated with the E₁ critical point (CP) of the Si substrate⁴¹; its strength is an indication of the film's transparency at that wavelength]. The spectral shift of the reflectivity peak between the treated and untreated AlN:Ag is evident for both wavelengths used for laser annealing.

The reflectivity peak at ~410 nm presented by the as-grown sample was verified to be originating from LSPR by variable angle Spectroscopic Ellipsometry²⁷. The spectral shift after LA of the reflectivity maximum is also accompanied by an increase of the absolute value of the peak reflectivity, which are is consistent with the bigger Ag nanoparticles observed after laser annealing (Fig. 3e,h). However, the LSPR bandwidth of the annealed sample at 193 nm is narrower, and the LSPR reflectivity maximum is stronger compared to those of the samples annealed at 248 nm. This is possibly due to the higher density of Ag nanoparticles and the more homogeneous size distributions of the bigger, annealed particles for the former case (see also Fig. 3e,h). This is a consequence of the more limited outdiffusion of Ag that is also implied by

the presented FDTD calculations for that case (Fig. 4c) showing reduced absorption, hence reduced heating, at 248 nm, compared to 193nm.

3.3 The effect of laser fluence

The data presented in Figs. 1a,b provide the reasonable suggestion that the laser fluence is an essential parameter for the laser annealing process and for controlling the plasmonic behavior of AlN:Ag templates. In order to investigate more systematically its effect, we performed a study by applying laser annealing with one pulse of 193 nm or two pulses of 248 nm at various fluences in the range 200-600 mJ/cm². Note that for the 248 nm wavelength we choose to apply two pulses based on the observations of Fig. 1c, *i.e.* two pulses provide the optimal plasmonic behavior of AlN:Ag.

The optical reflectivity spectra of the laser annealed AlN:Ag *vs.* the laser fluence for both processing wavelengths and the corresponding quantitative results are presented in Figs. 7 and 8, respectively. In the case of the 193 nm wavelength (Figs. 7a, 8a,b), it is evident that increasing the fluence from 200 mJ/cm² to 400 mJ/cm² induces a spectral shift and a significant enhancement of LSPR, which are respectively associated with changes of the matrix's refractive index and changes of the Ag nanoparticles size, respectively; the bandwidth (full width at half maximum of the Lorentzian curve used to fit the LSPR band), Fig 7b, is reduced with the laser fluence, indicating possibly a narrower size distribution of Ag nanoparticles due to the matrix crystallization, as well as to Ag particle enlargement causing weaker electronic confinement. Finally, at 600 mJ/cm² the reflectivity spectrum resembles that of pure Si proving that this fluence exceeds the ablation and lift-off threshold due to overheating of AlN:Ag.

On the other hand, for LA using two pulses at 248 nm the picture is quite different (Figs. 7b, 8c,d). At 300 mJ/cm² (Fig. 7b, magenta diamonds) the reflectivity spectrum is similar to the one pulse at 248 nm and 400 mJ/cm² (Fig. 1c), which is characterized by the absence of LSPR, indicating that the provided energy is not enough to cause ripening of Ag and only dissolution is observed. For fluences exceeding 400 mJ/cm², there is a consistent blue-shift of the LSPR, which can be explained only by the reduction of the refractive index of the surrounding medium, supporting the Ag outdiffusion to the free surface and the formation of Ag nanoparticles surrounded by air.

The experimental reflectivity spectra were fitted with a three-phase model (air/film/substrate). For the Si substrate we used the data of Palik³⁸, while the optical constants of the AlN:Ag films were modeled by the Maxwell-Garnett effective medium approximation⁴⁹ (MG-EMA); although MG-EMA might be considered as a simplified approach of this complex system, which incorporates surface and interface roughness and elongated Ag particles, provides straightforward results that are not affected by numerical issues that might affect more complex models of many variables. The MG-EMA fit consists of a single or double Lorentz model for the AlN matrix (the one Lorentzian describes the interband transition of AlN and the second is emerging only for laser annealed samples with high fluence of 193 nm; it is located at 3.2 eV/390 nm and can be associated with very small Ag nanoparticles outdiffused to the surface of the sample based on previous reports that the LSPR of Ag nanoparticles with size of less than 10 nm is manifested at 390 nm⁵⁰), and a Drude-Lorentz model for the Ag inclusions, which is however corrected for the reduced electron relaxation time τ due to surface scattering, approximated by⁵¹⁻⁵³, $\tau^{-1} = \tau_{bulk}^{-1} + A\nu_F/r$, where A is a unit-less phenomenological constant of order 1 accounting for different scattering conditions at the nanoparticle surface and/or interior

of the nanoparticle. Note that the A^{-1} can be also an account of particle enlargement after laser annealing; in fact, A adds contributions from the interfacial conditions and the Ag particle size as well, therefore, any deviation from reported values of A^{53} can be attributed mostly to Ag particle size variations. In our fit for the as-grown AlN:Ag we found $A=1.1$. After fitting the reflectivity results and analyzing the extracted parameters, we report a quantitative analysis regarding the LSPR spectral position (Fig. 8a,c) and bandwidth (Figs. 8b,d) and the refractive index of the dielectric matrix and the electron scattering parameter A of the metal in Figs. 9a,b. For the cases of laser annealing with the 193 nm laser (purple circles in Fig. 8) there is systematic red-shift due to the increase of the refractive index of the surrounding medium (see Fig. 9a, red open squares) because of the AlN crystallization around the Ag nanoparticles, in accordance with Ref. 27 and the FDTD results of Fig. 4c.

Significant insights can be extracted from the data presented in Fig. 9; to better visualize the data, we split them in two families, the single pulse family and the multi-pulse family. The common x-axis for both is total incident energy. It is worth noting that larger single-pulse energy causes a higher index change from that caused by multi pulses, even if their total energy exceeds that of the single pulse. This is very well understood taking into account the FDTD results (Fig. 4c) and the melting point of AlN (2750 °C)⁵⁴: single pulse processing delivers higher absolute energy during the pulse, resulting into a higher temporal temperature which might reach the melting point of AlN and cause recrystallization. For multi-pulse processing, on the other hand, the effective temperature during the pulse is lower, and thus the index enhancement due to AlN crystallization is more moderate. These findings open the pathway for employing other nitride matrices with similar melting points, such as BN and GaN⁵³ and the index-sensitive $Al_xGa_{1-x}N$ alloys, for similar plasmonic applications. On the other hand, the Ag electron scattering factor A

is scaled with the total delivered energy and not with the maximum intensity of the laser beam; we attribute this behavior to the relative low melting point of Ag (961 °C)⁵⁵, that can be reached even by low fluence annealing; then, the diffusion-based enlargement of Ag, which is associated with the Ag particle diameter, will be a cumulative result of the total energy delivered to the system. Note also, that the particle enhancement is considered vertically to the direction of the propagation of the laser beam, *i.e.* parallel to the film surface and to the axis of the electric field of laser. Thus, even elongation of particles along these axes, as observed in the TEM image of Fig. 3e, will have similar optical effect.

The dominant effects of index enhancement and particle enlargement are accompanied by a secondary peak at 390 nm manifested for high fluence (400 mJ/cm²) at 193 nm. This is due to outdiffusion of Ag and the formation of very fine (<10 nm) nanoparticles, showing that the outdiffusion of Ag can take place also by increasing the fluence. The Ag outdiffusion seems also to be the dominant effect of the 248 nm laser annealing for fluences exceeding 400 mJ/cm² (Fig. 8c, magenta diamonds and magenta arrow), due to overheating of the Ag nanoparticles (Fig. 8c, magenta arrow). Further evidence for the different fundamental effects occurring during 193 nm or 248 nm laser annealing is provided by the bandwidth of the LSPR peak (Fig. 8b,d); indeed, the increasing bandwidth with the fluence for 248 nm laser annealing can be explained by the size polydispersity of outdiffused Ag, while the reducing bandwidth with the fluence for 193 nm may indicate that the AlN crystallization stabilizes Ag to a narrower size distribution.

3.4 Application – Optical Encoding

The structural modifications introduced by laser annealing in AlN:Ag and the variation of AlN:Ag's plasmonic response form clear evidence that the optical behavior of these films can be

strongly spectrally sensitive. In order to examine this possibility we encoded the patterns “ALN:AG”, “ALN”, and “AL” onto films of AlN:Ag, AlN and Al, respectively, deposited either on Si or sapphire substrates, using either the 193 nm or the 248 nm beam for annealing, and their response to different light colors was investigated using optical microscopy.

The reflectivity contrast $\Delta R (=R_{LA} - R_{untreated})$ between the treated and untreated parts of an AlN:Ag sample demonstrates the level of contrast the human eye can resolve; the spectral variations of such ΔR contrasts for 193 nm and 248 nm laser annealing are presented in Fig. 10a (purple and magenta points, respectively) for all cases of laser treated AlN:Ag deposited on opaque Si substrates and presented previously in Figs. 1 and 7. It can be seen that depending on the processing wavelength and laser annealing conditions (fluence and number of pulses), exceptional flexibility in selecting the required encoding ΔR contrast over the whole visible spectral range can exist. In particular, the spectral selectivity is greater when large variations of ΔR are manifested in the visible spectrum. For example, for laser annealing using one pulse of 400 mJ/cm² of 193 nm (Fig. 10a, solid purple diamonds) the ΔR ranges from 5% for red (650 nm) to 35% for blue (475 nm) providing very strong spectral selectivity. This is also demonstrated in the inset of Fig 10a, where an optical microscopy image under fluorescent light white illumination of a pattern formed by LA at 193 nm (one pulse of 400 mJ/cm²) using a standard lithographic mask is shown. Note that the laser annealed area appears in bright blue where the maximum of ΔR is observed. These conditions are ideal for spectrally sensitive overt encoding. On the contrary, covert encoding requires more subtle spectral contrast ΔR in order the pattern to be invisible under white light illumination and be revealed only under the colored illumination in the LSPR region. This can be done by, *e.g.*, laser annealing using two pulses of 500 mJ/cm² of 248 nm (Fig. 10a, solid magenta triangles).

The potential of the present plasmonic encoding is better demonstrated by optical microscopy images, where the sample is illuminated by different colored light [for the optical microscopy demonstration we used the standard components of the RGB scheme: blue/468 nm, green/532 nm, red/655 nm; the corresponding emission spectra of the three illumination sources are shown in Fig. 10b]. For this demonstration we used AlN:Ag, AlN and Al films grown on transparent sapphire substrates in order to evaluate both the reflection and transmission reading; the relevant optical microscopy images are presented in Fig. 11. In particular, images A1-D1 correspond to covert encoding realized by laser annealing of AlN:Ag at 248 nm in transmission reading. The pattern (pixel size 60 μm) is almost invisible under white light illumination (A1) and it is revealed only under blue illumination (D1) where LSPR is manifested. Images A2-D2 and A3-D3 correspond to overt encoding realized by laser annealing at 193 nm in transmission and reflection reading, respectively. The pixels reflect an average cyan color (A3) but let the red, which is far away from LSPR, to pass through (A2), thus creating a different appearance in reflection and transmission reading (this might be seen as the micro-scale equivalent of the Lycurgus cup). These laser-induced patterns are indeed spectrally sensitive. For example the ‘ALN:AG’ pattern, encoded with the 193 nm wavelength (Fig. 11, images A3-D3), is visible when blue illumination is used (D3) and barely visible for green (C3), whereas invisible for red illumination (B3). The spectral sensitivity of the plasmonic patterns (A1-D1, A2-D2, A3-D3) contrasts the behavior of patterns encoded by laser ablation in AlN (images A4-D4) and in Al (images A5-D5), which do exhibit similar contrasts for all colors, mostly due to scattering of light at the pixel edges.

In addition to photosensitivity, AlN:Ag films have a unique combination of assets such as being harder than steel⁴⁶, chemically resistant against organic solvents (they have endured dipping and

stirring into the most aggressive solvents, see online supplementary data for more details), almost having pitchless surface²⁷ and are resistant to temperatures up to 600 °C⁴¹. Although the presented patterning process was previously demonstrated for minimum feature size around 1.5 μm ²⁷, the underlying plasmon-relevant structural changes can be much finer. Indeed, the diameter of the Ag PNPs is more than fifty times smaller than the diffraction limit of the laser wavelength used for patterning in this work (193 nm and 248 nm). This provides exceptional perspectives for overt and covert encoding of durable, spectrally-sensitive, and miniature patterns that could revolutionize forensics, cryptography and authentication patterning.

5. Conclusions

The photosensitivity of AlN:Ag plasmonic nanocomposites was thoroughly studied and a series of UV laser annealing parameters, such as the laser wavelength (193 nm or 248 nm), fluence (200-600 mJ/cm²) and number of pulses (1-5) were investigated. Based on detailed electron microscopy and spectroscopy experiments, we identified the fundamental physicochemical processes taking place during laser-driven modifications in AlN:Ag, which was used as an archetypical example of a composite of a III-nitride wide band-gap semiconductor with noble metal inclusions. We observed the selective crystallization of AlN matrix, that takes place only in the AlN:Ag nanocomposites and not in pure AlN, demonstrating the important role of the Ag nanoparticles in the photosensitivity of starting material. Additionally we report the enlargement of Ag nanoparticle inclusions by diffusion of laser-heated Ag, which can have a dramatic effect in both tuning and enhancing the LSPR signal observed from the thin film. Crucially and on demand, this effect can also be limited by choosing appropriate laser processing parameters, enabling the accurate fabrication of contrasting areas, thus creating a desired image. Finally we also report the outdiffusion of Ag to the film's surface, which occurs beyond a certain higher

level of laser processing (higher fluence and/or number of pulses), as well as a critical lower level of laser processing required for the onset of the induced changes. Based on MG-EMA fits of the optical reflectivity spectra, we identified that the matrix crystallization scales to the laser power, while the Ag diffusion effects scale to the total laser energy delivered to the sample. This discrimination between the matrix and Ag open the way for implementation of other transparent III-nitrides with similar melting points such as BN, GaN and $\text{Al}_x\text{Ga}_{1-x}\text{N}$, which might provide even more versatility in the tuning of matrix's index. Detailed FDTD calculations performed revealed the paramount role of all components involved (AlN host, Ag nanoparticles and Si substrate). All calculations have contributed to the identification and understanding of the aforementioned physical mechanisms, and thus enlist them in the production of a proof-of-principle demonstrator of an image optically encoded in an AlN:Ag nanocomposite. We demonstrated the novel photosensitivity of inorganic nanocomposite films which can be engineered to provide two views of the same image with complementary colors in reflection and transmission (overt in white light), or alternatively an image that is resolved to the human eye only when illuminated with a specific color light source (covert in white light).

6. Acknowledgements

The XPS/XAES and SEM experiments were performed in the Central Surface Science Facility of the Aristotle University of Thessaloniki and the Central Scanning Electron Microscopy Facility of the University of Ioannina, respectively. All calculations were performed on the 192-cpu in-house Beowulf computer cluster VIKOS in the Materials Science and Engineering Department at the University of Ioannina.

This work has been co-funded by the European Union - European Social Fund (ESF) & National Sources, in the framework of the program “HERAKLEITOS II” of the “Operational Program Education and Life Long Learning” of the Hellenic Ministry of Education, Life-Long Learning and Religious Affairs.

REFERENCES

- ¹Maier, SA *Plasmonics: Fundamentals and Applications* 2007 Springer Science and Business Media LLC, New York, pp 65-87.
- ²Brongersma ML, Shalaev VM, The Case for Plasmonics 2010 *Science* 328, 440-441.
- ³Fan JA, Wu C, Bao K, Bao J, Bardhan R, Halas NJ, Manoharan, VN, Nordlander P, Shvets G, Capasso F, Self-Assembled Plasmonic Nanoparticle Clusters 2010 *Science* 328, 1135-1138.
- ⁴Halas NJ, Plasmonics: An Emerging Field Fostered by Nano Letters 2010 *Nano Lett.* 10, 3816-3822.
- ⁵Lu X, Rycenga M, Skrabalak SE, Wiley BJ, Xia Y, Chemical Synthesis of Novel Plasmonic Nanoparticles 2009 *Ann. Rev. Phys. Chem.* 60, 167-192.
- ⁶Ozbay E, Plasmonics: Merging Photonics and Electronics at Nanoscale Dimensions 2006 *Science* 311, 189-193.
- ⁷Van Duyne RP, Molecular Plasmonics 2004 *Science* 306, 985-986.
- ⁸Barnes WL, Dereux A, Ebbesen TW, Surface Plasmon Subwavelength Optics 2003 *Nature* 424, 824-830.
- ⁹Larsson EM, Langhammer C, Zoric I, Kasemo B, Nanoplasmonic Probes of Catalytic Reactions 2009 *Science* 326, 1091-1094.
- ¹⁰Atwater HA, Polman A, Plasmonics for Improved Photovoltaic Devices 2010 *Nature Mater.* 9, 205-213.
- ¹¹Aubry A, Lei DY, Fernandez-Dominguez AI, Sonnefraud Y, Maier SA, Pendry JB, Plasmonic Light-Harvesting Devices over the Whole Visible Spectrum 2010 *Nano Lett.* 10, 2574-2579.
- ¹²Ozaki M, Kato J-I, Kawata S, Surface-Plasmon Holography with white-light illumination 2011 *Science* 332, 218-220.

- ¹³Nakashima S, Sugioka K, Midorikawa K, Mukai K, Spatially Selective Modification of Optical and Magneto-Optical Properties in Fe- and Au-doped Glasses Irradiated with Femtosecond-Laser 2013 *Appl. Phys. A*. 110, 765-769.
- ¹⁴Doster J, Baraldi G, Gonzalo J, Solis J, Hernandez-Rueda J, Siegel J, Tailoring the surface plasmon resonance of embedded silver nanoparticles by combining nano- and femtosecond laser pulses 2014 *Appl. Phys. Lett.* 104, 1531061-1531064.
- ¹⁵Jin R, Cao YW, Mirkin CA, Kelly KL, Schatz GC, Zheng JG, Photoinduced Conversion of Silver Nanospheres to Nanoprisms 2001 *Science* 294, 1901-1903.
- ¹⁶Chon JWM, Bullen C, Zijlstra P, Gu M, Spectrum Encoding on Gold Nanorods Doped in Silica Sol-Gel Matrix and its Application to High Density Optical Data Storage 2007 *Adv. Funct. Mater.* 17, 875-880.
- ¹⁷Chen X, Chen Y, Yan M, Qiu, M, Nanosecond Photothermal Effects in Plasmonic Nanostructures 2012 *ACS Nano* 6, 2550-2557.
- ¹⁸Warth A, Lange J, Graener H, Seifert G, Ultrafast Dynamics of Femtosecond Laser Induced Shape Transformation of Silver Nanoparticles Embedded in Glass 2011 *J. Phys. Chem. C* 115, 23329-23337.
- ¹⁹Stalmashonak A, Graener H, Seifert G, Transformation of Silver Nanospheres Embedded in Glass into Nanodisks Using Circularly Polarized fs Pulses 2009 *Appl. Phys. Lett.* 94, 1931111-1931113.
- ²⁰Unal AA, Stalmashonak A, Seifert G, Graener H, Ultrafast Dynamics of Silver Nanoparticle Shape Transformation Studied by Femtosecond Pulse-pair Irradiation 2009 *Phys. Rev. B* 79, 1154111-1154117.

- ²¹Sanchez-Valencia JR, Toudert J, Borrás A, Barranco A, Lahoz R, de la Fuente GF, Frutos F, Gonzalez-Elipe AR, Selective Dichroic Patterning by Nanosecond Laser Treatment of Ag Nanostripes 2011 *Adv. Mater.* 23, 848-853.
- ²²Grochowska K, Śliwiński G, Iwulska A, Sawczak M, Nedyalkov N, Atanasov P, Obara G, Obara M, Engineering Au Nanoparticle Arrays on SiO₂ Glass by Pulsed UV Laser Irradiation 2013 *Plasmonics* 8, 105-113.
- ²³Stepanov AL, Nuzhdin VI, Valeev VF, Kreibig U 2010 Optical Properties of Metal Nanoparticles. *Proc. of SPIE* 7993, No. 79931Y.
- ²⁴Beliatis MJ, Henley SJ, Silva SRP, Engineering the Plasmon Resonance of Large Area Bimetallic Nanoparticle Films by Laser Nanostructuring for Chemical Sensors 2011 *Opt. Lett.* 36, 1362-1364.
- ²⁵Beliatis MJ, Martin NA, Leming EJ, Silva SRP, Henley SJ, Laser Ablation Direct Writing of Metal Nanoparticles for Hydrogen and Humidity Sensors 2011 *Langmuir* 27, 1241-1244.
- ²⁶Halabica A, Idrobo JC, Pantelides ST, Magruder RH, Pennycook SJ, Haglund RF Jr, Pulsed Infrared Laser Annealing of Gold Nanoparticles Embedded in a Silica Matrix 2008 *J. Appl. Phys.* 103, No. 083545.
- ²⁷Siozios A, Koutsogeorgis DC, Lidorikis E, Dimitrakopoulos GP, Kehagias T, Zoubos H, Komninou P, Cranton WM, Kosmidis C, Patsalas P, Optical Encoding by Plasmon-Based Patterning: Hard and Inorganic Materials Become Photosensitive 2012 *Nano Lett.* 12, 259-263.
- ²⁸Zijlstra P, Chon JWM, Gu M, Five-Dimensional Optical Recording Mediated by Surface Plasmons in Gold Nanorods 2009 *Nature* 459, 410-413.

- ²⁹Wan D, Chen H-L, Tseng S-C, Wang LA, Chen Y-P, One-Shot Deep-UV-Pulsed Laser-Induced Photomodification of Hollow Metal Nanoparticles for High Density Data Storage on Flexible Substrates 2010 *ACS Nano* 4, 165-173.
- ³⁰Royon A, Bourhis K, Bellec M, Papon G, Bousquet B, Deshayes Y, Cardinal T, Canioni L, Silver Clusters Embedded in Glass as a Perennial High Capacity Optical Recording Medium 2010 *Adv. Mater.* 22, 5282-5286.
- ³¹Stalmashonak A, Abdolvand A, Seifert G, Metal-Glass Nanocomposite for Optical Storage of Information 2011 *Appl. Phys. Lett.* 99, No. 201904.
- ³²Chen WT, Wu PC, Chen CJ, Weng C-J, Lee H-C, Yen T-J, Kuan C-H, Mansuripur M, Tsai DP, Manipulation of Multidimensional Plasmonic Spectra for Information Storage 2011 *Appl. Phys. Lett.* 98, No. 171106.
- ³³Kumar K, Duan H, Hegde RS, Koh SCW, Wei JN, Yang JKW, Printing Colour at the Optical Diffraction Limit 2012 *Nature Nanotech.* 7, 557-561.
- ³⁴Taylor AB, Kim J, Chon JWM, Detuned Surface Plasmon Resonance Scattering of Gold Nanorods for Continuous Wave Multilayered Optical Recording and Readout 2012 *Opt. Express* 20, 5069-5081.
- ³⁵Matenoglou GM, Evangelakis GA, Kosmidis C, Foulis S, Papadimitriou D, Patsalas P, Pulsed Laser Deposition of Amorphous Carbon/Silver Nanocomposites 2007 *Appl. Surf. Sci.* 253, 8155-8159.
- ³⁶Panagiotopoulos NT, Diamanti EK, Koutsokeras LE, Baikousi M, Kordatos E, Matikas TE, Gournis D, Patsalas P, Nanocomposite Catalysts Producing Durable, Super-Black Carbon Nanotube Systems: Applications in Solar Thermal Harvesting 2013 *ACS Nano* 6, 10475-10485.

- ³⁷Taflove A, Hagness SC, *Computational electrodynamics: The finite-difference time-domain method* 2005 Artech House, Inc.: Norwood.
- ³⁸Palik ED, *Handbook of Optical Properties of Solids III* 1998 Academic Press: San Diego, pp 531-533.
- ³⁹Lidorikis E, Egusa S, Joannopoulos JD, Effective medium properties and photonic crystal superstructures of metallic nanoparticle arrays 2007 *J. Appl. Phys.* 101, No. 054304.
- ⁴⁰Kreibig U, Von Fragstein C, The limitation of electron mean free path in small silver particles. 1969 *Z. Phys.* 224, 307-323.
- ⁴¹Siozios A, Zoubos H, Pliatsikas N, Koutsogeorgis DC, Vourlias G, Pavlidou E, Cranton W, Patsalas P, Growth and Annealing Strategies to Control the Microstructure of AlN:Ag Nanocomposite Films for Plasmonic Applications 2014 *Surf. Coat. Technol.* 255, 28-36.
- ⁴²Lautenschlager P, Garriga M, Viña L, Cardona M, Temperature Dependence of the Dielectric Function and Interband Critical Points in Silicon 1987 *Phys. Rev. B* 36, 4821-4830.
- ⁴³Redmond PL, Hallock AJ, Brus LE, Electrochemical Ostwald Ripening of Colloidal Ag Particles on Conductive Substrates 2005 *Nano Lett.* 5, 131-135.
- ⁴⁴Palmberg PW, Rhodin TN, Auger Electron Spectroscopy of fcc Metal Surfaces 1968 *J. Appl. Phys.* 39, 2425-2432.
- ⁴⁵Gallon TE, A Simple Model for the Dependence of Auger Intensities on Specimen Thickness 1969 *Surf. Sci.* 17, 486-489.
- ⁴⁶Beszeda A, Gontier-Moya EG, Imre AW, Surface Ostwald-ripening and evaporation of gold beaded films on sapphire 2005 *Appl. Phys. A* 81, 673-677.

- ⁴⁷Lotsari A, Dimitrakopoulos GP, Kehagias T, Kavouras P, Zoubos H, Koutsokeras LE, Patsalas P, Komninou P, Structure, Stability and Mechanical Performance of AlN:Ag Nanocomposite Films 2010 *Surf. Coat. Technol.* 204, 1937-1941.
- ⁴⁸Matenoglou GM, Zoubos H, Lotsari A, Lekka CE, Komninou P, Dimitrakopoulos GP, Kosmidis C, Evangelakis GA, Patsalas P, Metal-Containing Amorphous Carbon (a-C:Ag) and AlN (AlN:Ag) Metallo-Dielectric Nanocomposites 2009 *Thin Solid Films* 518, 1508-1511.
- ⁴⁹Maxwell-Garnett JC, Colours in Metal Glasses and in Metallic Films 1904 *Philos. Trans. R. Soc. London, Ser. A* 203, 385-420.
- ⁵⁰Amendola V, Bakr OM, Stellacci F, A Study of the Surface Plasmon Resonance of Silver Nanoparticles by the Discrete Dipole Approximation Method: Effect of Shape, Size, Structure, and Assembly 2010 *Plasmonics* 5, 85-97.
- ⁵¹Kreibig U, Electronic Properties of Small Silver Particles: The Optical Constants and their Temperature Dependence 1974 *J. Phys. F: Met. Phys.* 4, 999-1014.
- ⁵²Matenoglou GM, Koutsokeras LE, Lekka CE, Abadias G, Camelio S, Evangelakis GA, Kosmidis C, Patsalas P, Optical Properties, Structural Parameters, and Bonding of Highly Textured Rocksalt Tantalum Nitride Films 2008 *J. Appl. Phys.* 104, No. 124907.
- ⁵³Kreibig U, Bour G, Hilger A, Gartz M, Optical Properties of Cluster-Matter: Influences of Interfaces 1999 *Phys. Stat. Sol. A* 175, 351-366.
- ⁵⁴Levinshtein ME, Romyantsev SL, Shur MS, *Properties of Advanced Semiconductor Materials GaN, AlN, InN, BN, SiC, SiGe* 2001 John Wiley & Sons, New York, pp. 31-47.
- ⁵⁵Haynes WM, *CRC Handbook of Chemistry and Physics, 95th ed.* 2014 CRC Press: Boca Raton.

FIGURE CAPTIONS

Figure 1: Optical reflectivity spectra for 1, 2 and 5 successive pulses for laser annealing using: (a) 193 nm wavelength, 200 mJ/cm² fluence, (b) 193 nm wavelength, 400 mJ/cm² fluence, and (c) 248 nm wavelength, 400 mJ/cm² fluence.

Figure 2: The relative intensity of the derivative Ag_{MNN} XAES peak vs. the number laser pulses used for annealing for the two used wavelengths.

Figure 3: Cross section TEM images of increasing resolution of AlN:Ag/Si: (a,b,c) as-grown, (d,e,f) laser annealed with one pulse of 193 nm/400 mJ/cm², and (g,h,i) laser annealed with two pulses of 248 nm/400 mJ/cm².

Figure 4: (a) Absorption distribution as a function of depth for a 60 nm thick AlN:Ag(15% vol)/Si system. (b) Absorption percentages for each material within the AlN:Ag/Si system. The rest of the energy to 100% is the reflection (c) Color coded absorption distribution maps.

Figure 5: Absorption percentage within each material as a function of nanoparticle size, for (a) 193 nm and (b) 248 nm laser annealing wavelengths. The semi-open circles at 20 nm size correspond to the nanoparticles having a non-absorbing 2.5 nm crystalline AlN (n=2.1) shell around them. Note that only ordered arrays of Ag NPs are considered here for simplicity, and so there may be a small numerical difference from the results of Fig. 3 regarding the 3 nm Ag NPs.

Figure 6: Optical reflectivity of AlN:Ag: as grown (black diamonds), LA with a 193 nm-400 mJ/cm² pulse (purple triangles), and LA with two 248 nm-400 mJ/cm² pulses (magenta circles);

the optical reflectivity of the Si substrate is demonstrated by the black line for comparison purposes, especially for the E_1 critical point (CP) manifested at ~ 365 nm.

Figure 7: Optical Reflectivity spectra with respect to laser fluence for LA at (a) 1 pulse at 193 nm and (b) 2 pulses at 248 nm.

Figure 8: The results of the quantitative analysis based on MG-EMA regarding the (a) LSPR spectral position, and (b) LSPR bandwidth for 193 nm LA and (c), (d) for 248 nm LA, respectively; the lines are guides to the eye.

Figure 9: The two optical parameters of AlN:Ag that strongly vary with the laser annealing: (a) the refractive index of the AlN at 532 nm (center of the visible spectrum), and (b) the electron relaxation time parameter A for Ag.

Figure 10: (a) Spectral reflectivity contrasts (ΔR) for laser annealing of AlN:Ag on Si (opaque substrate) at 193 and 248 nm (purple and magenta lines, respectively) for various number of pulses and fluences demonstrating the flexibility in selecting the required encoding contrast; the inset shows an optical microscopy image under fluorescent white light illumination of a pattern formed by LA at 193 nm (1 pulse of 400 mJ/cm^2) using a standard lithographic mask (note that the laser annealed area appears in bright blue where the maximum of ΔR is observed). (b) The emission spectra of the three Red-Green-Blue (RGB) light sources used for optical microscopy observations.

Figure 11: Optical microscopy images of AlN:Ag, AlN, Al on sapphire using A. white, B. red, C. Green, and D. blue illumination, in transmission (1,2) or reflection (3,4,5) mode on sapphire for 248 nm (1), and 193 nm (2-5) laser annealing, respectively.

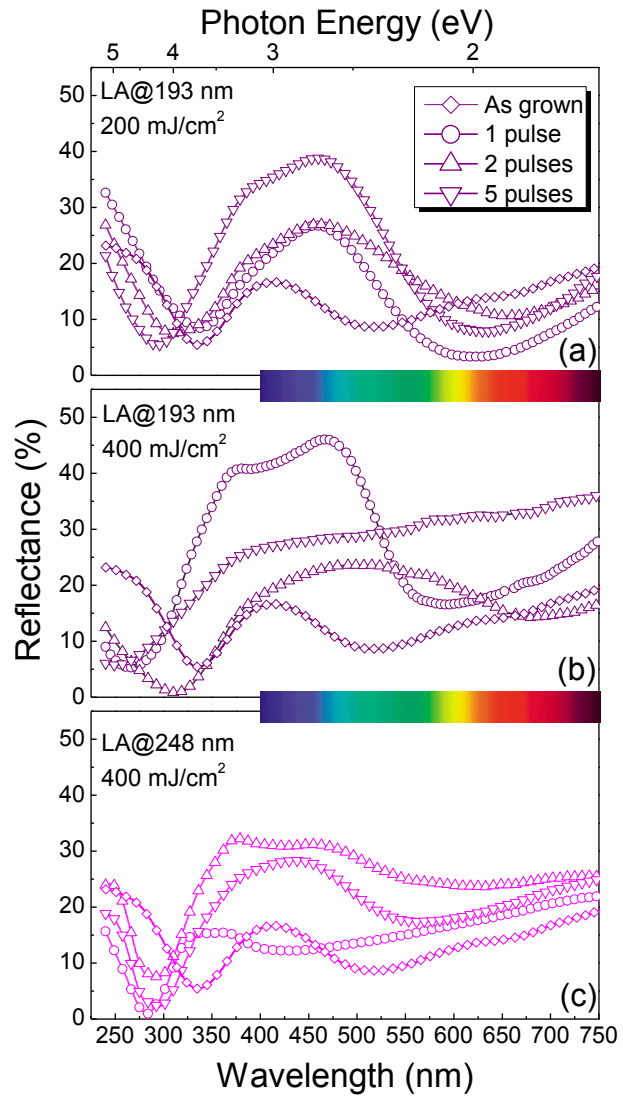


Figure 1

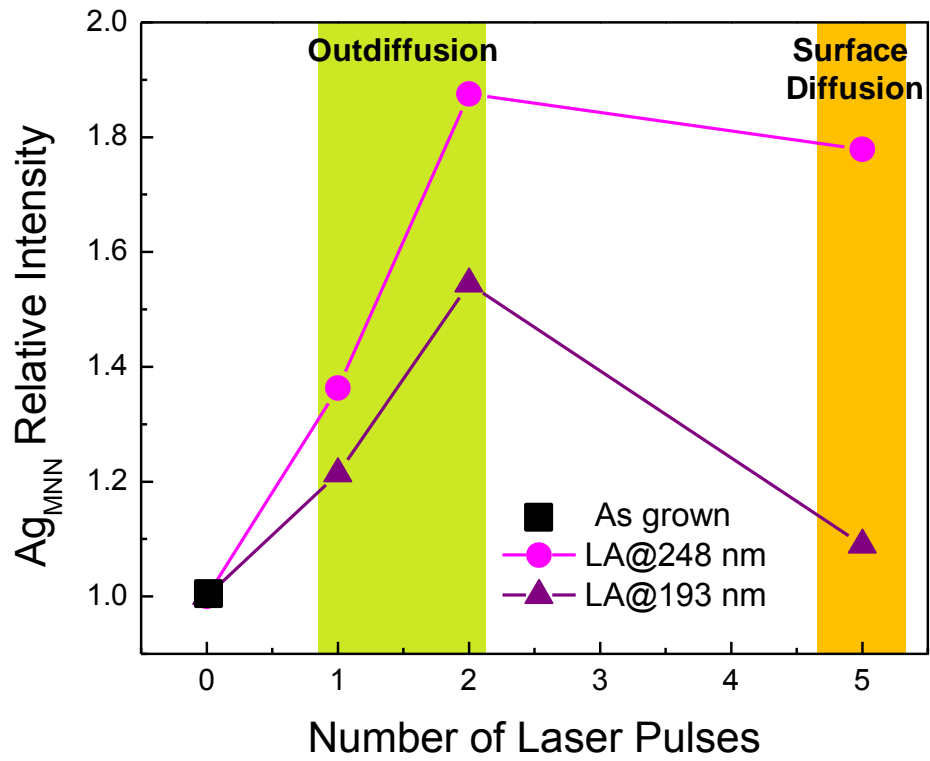


Figure 2

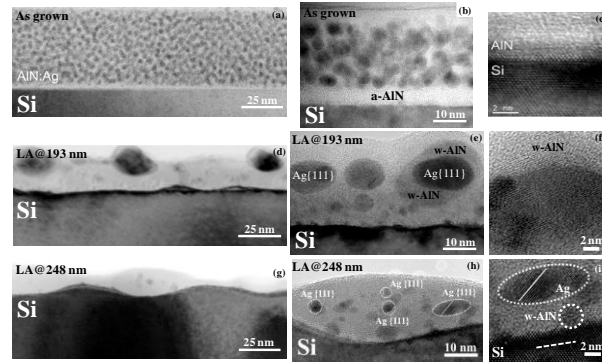


Figure 3

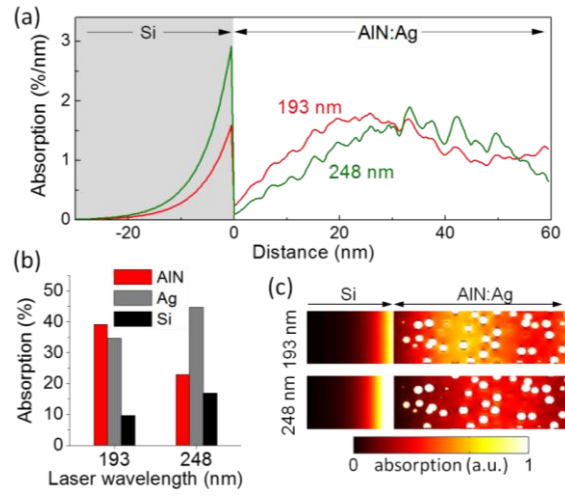


Figure 4

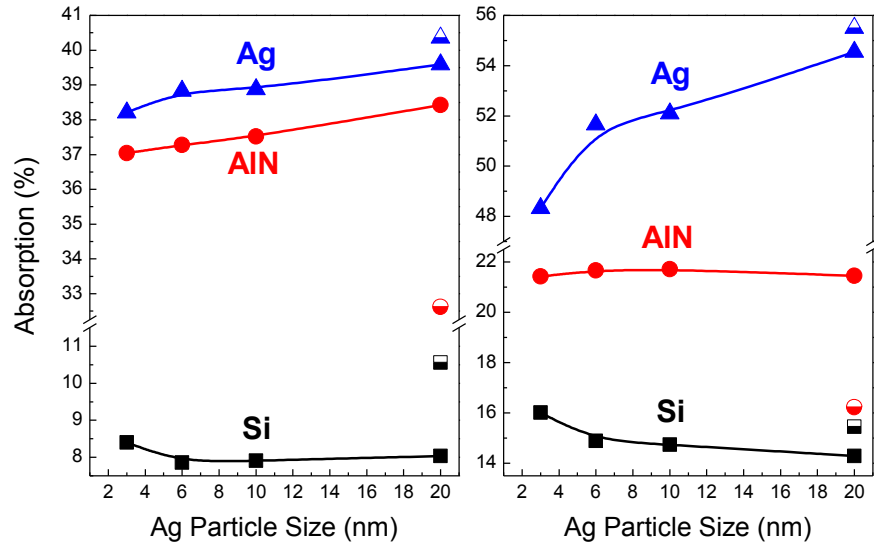


Figure 5

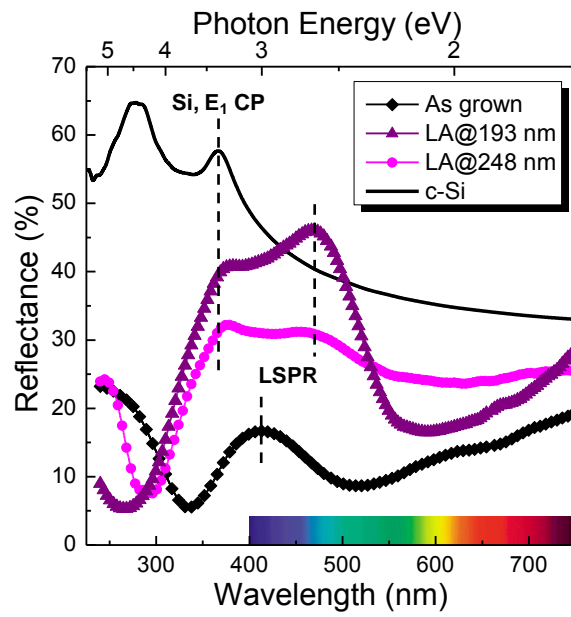


Figure 6

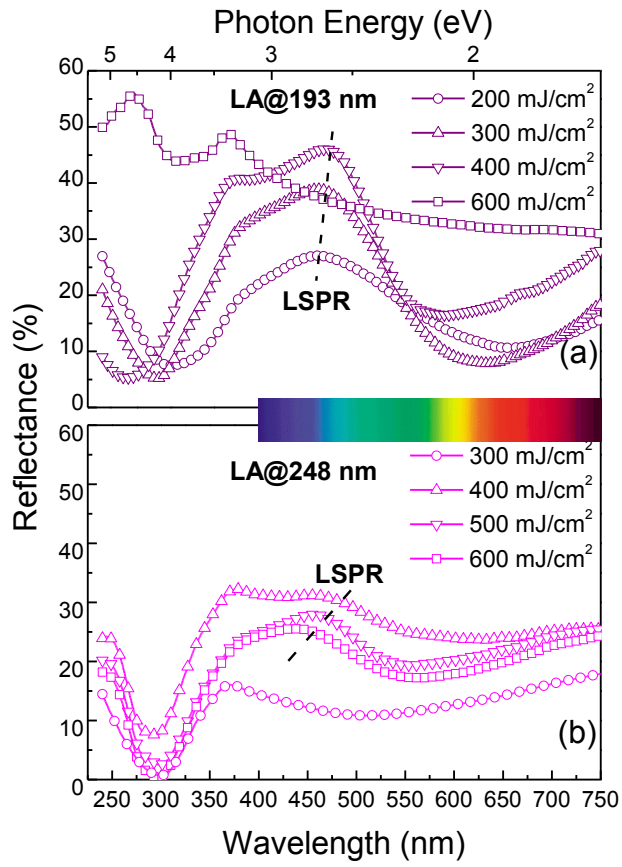


Figure 7

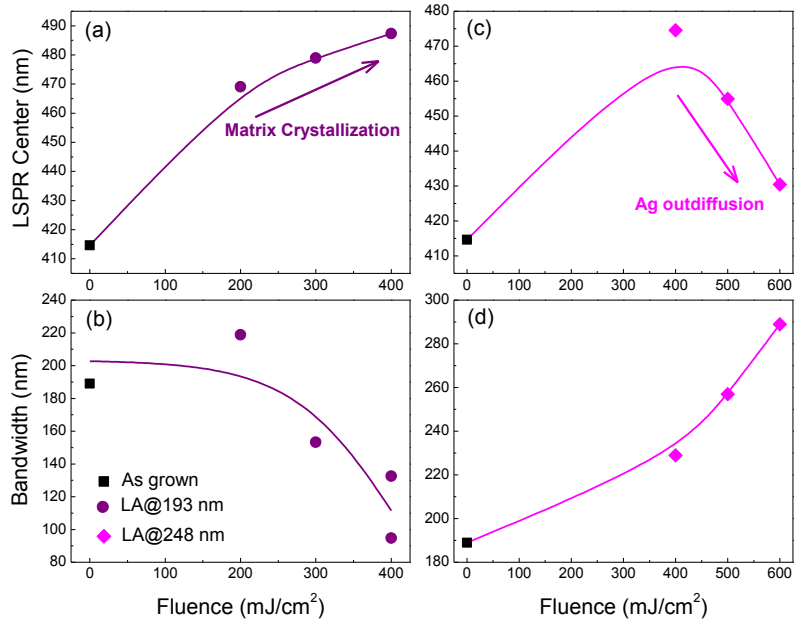


Figure 8

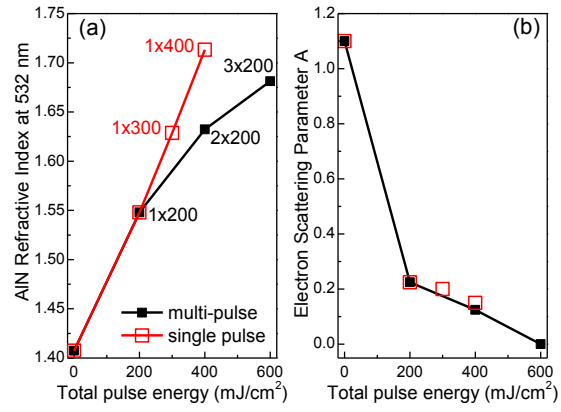


Figure 9

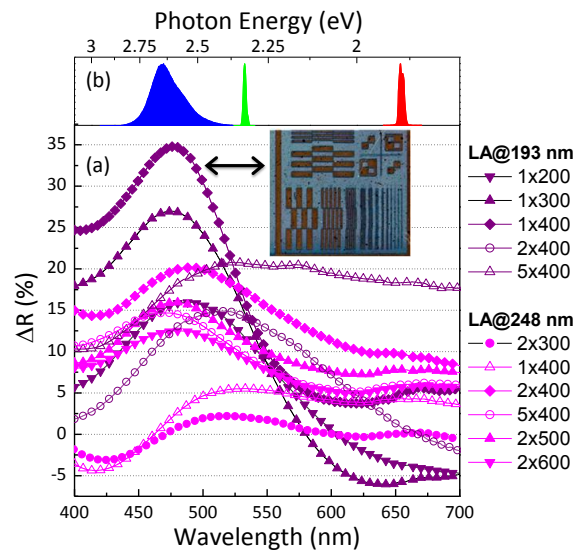


Figure 10

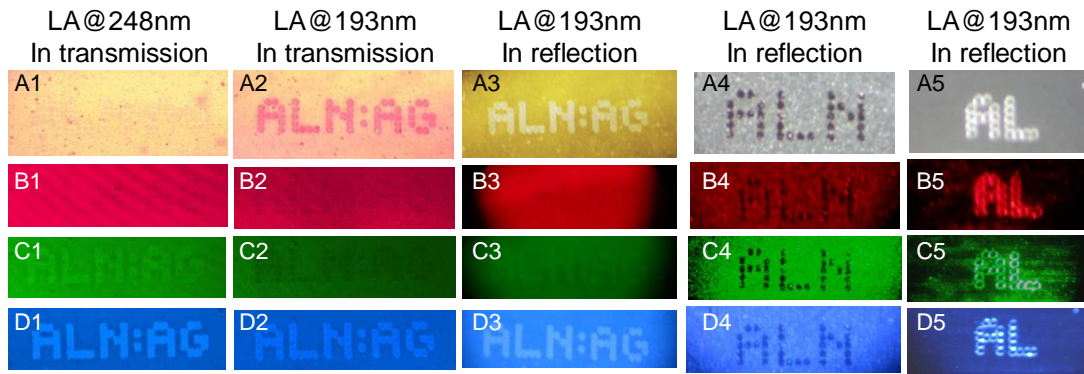


Figure 11

SUPPLEMENTARY DATA

Provided in the following pages

Laser-matter interactions, phase changes and diffusion phenomena during laser annealing of plasmonic AlN:Ag templates and their applications in optical encoding

Anastasios Siozios¹, Demosthenes C.Koutsogeorgis², Elefterios Lidorikis¹, George P. Dimitrakopoulos³, Nikolaos Pliatsikas³, Georgios Vourlias³, Thomas Kehagias³, Philomela Komninou³, Wayne Cranton^{2,4}, Constantine Kosmidis⁵, and Panos Patsalas^{1,3,*}

¹*University of Ioannina, Department of Materials Science and Engineering, GR-45110 Ioannina, Greece*

²*Nottingham Trent University, School of Science and Technology, NG11 8NS, Nottingham, UK*

³*Aristotle University of Thessaloniki, Department of Physics, GR-54124 Thessaloniki, Greece*

⁴*Sheffield Hallam University, Materials and Engineering Research Institute, Sheffield, S1 1WB, UK*

⁵*University of Ioannina, Department of Physics, GR-45110 Ioannina, Greece*

**Corresponding Author, e-mail: ppats@physica.auth.gr, tel: +30-2310-998298*

1. Laser annealing of AlN/Si

We show here that the reported photosensitivity is a property of the composite AlN:Ag system and cannot be reproduced by the host alone. To do so, we study the interaction of the laser beam with a pure AlN film deposited by PLD on a Si(100) substrate, and evaluate the potential structural and morphological changes upon laser annealing. Figure S1a shows the optical reflectivity spectra of an as-grown AlN/Si sample (solid black circles) together with the after-laser annealing spectra using the 248 nm laser beam (magenta up- and down-triangles for 400 and 500 mJ/cm² respectively, denoted as LA@248 nm) and the 193 nm laser beam (purple up- and down- triangles and diamonds

for 100, 300 and 400 mJ/cm² respectively, denoted as LA@193 nm). It is evident that for low fluence (LA@193 nm 100 mJ/cm²) the changes in the optical reflectivity spectra are minor and may be attributed to the Si interface roughening and amorphization due to direct laser energy delivery to the substrate, consistent with the laser beam not interacting with the AlN layer itself because of its relative transparency; note that the fundamental gap of our AlN was found by spectroscopic ellipsometry to be above E_g=6.2 eV (photon energy at λ=193 nm is ~6.42 eV), a value that is in good agreement with other reported literature (see W.M. Yim et al, J. Appl. Phys. 1974, 44, 292-296 and J. Li et al, Appl. Phys. Lett. 2003, 83, 5163-5165).

For higher fluences that are comparable to the laser damage threshold of Si (which has been reported to be about 350 mJ/cm² when a 248 nm laser beam was used, see F. Beaudoin et al, J. Vac. Sci. Technol. A 1998, 16, 1976 and H. Aoshima et al, Phys. Stat. Sol. C 2012, 9, 753-756), the AlN film is removed exposing the underlying Si, as it is shown by the characteristic Si-relevant reflectivity peak at about 330 nm (Fig. S1a) and in the secondary electron plane-view images (Fig. S1b,c). The chemistry of the treated and the untreated areas has been evaluated in the SEM by energy dispersive X-ray spectroscopy. Given the AlN film transparency, it is evident that the lift-off⁴⁰ mechanism involves the damage of the underlying Si and the thermal and pressure build-up at the AlN/Si interface. On the contrary, the AlN:Ag/Si samples endured the laser irradiation (193 nm, 300 mJ/cm²), as shown in the plane view secondary electron image of Fig. S1d, with no AlN:Ag removal observed (the horizontal red line denotes the border between the treated and untreated areas of the sample's surface); the film remained intact and only its reflectivity changed after laser annealing. This is because the Ag nanoparticles absorb and scatter the incoming laser reducing thus the light intensity delivered to the Si substrate below its damage threshold. This will be discussed in more detail in the following sections.

Finally, for even higher laser fluences (500 mJ/cm² at 248 nm and 400 mJ/cm² at 193 nm) besides the AlN removal, a broadening of the Si peak at 330 nm is observed, due to Si damage and

amorphization to a larger extent. As an overall conclusion, the radiation of pure AlN by intense UV pulsed laser beams does not alter the structural features of the films, because the damage threshold of the Si substrate is below the corresponding annealing threshold of AlN and hence it cannot be reached without totally ablating the film.

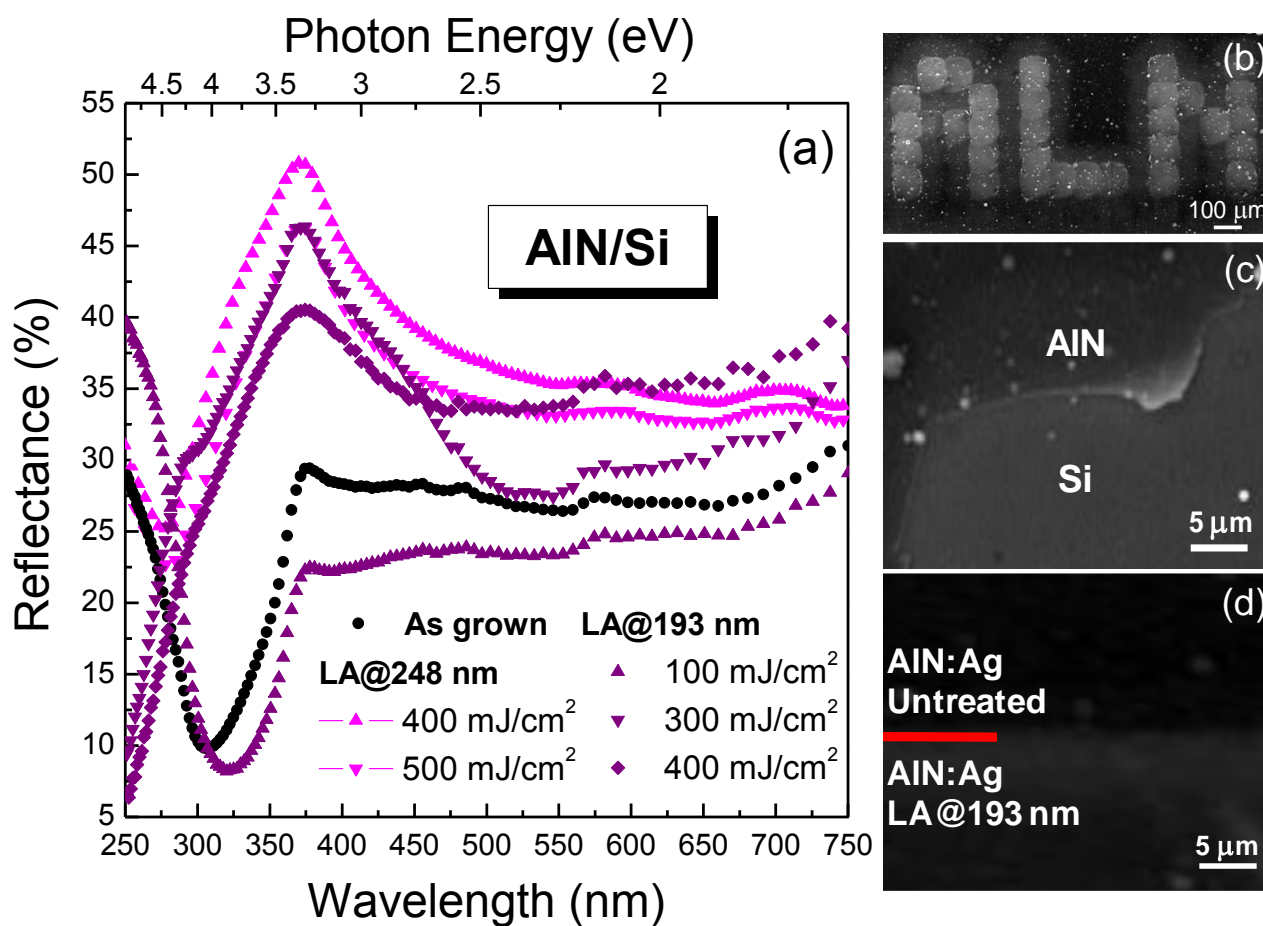


Figure S1: (a) Optical reflectance spectra of AlN/Si as grown, LA@193 nm and LA@248 nm vs. laser fluence, (b) a secondary electron image from an AlN/Si sample where the pattern ‘ALN’ has been lift-off by a 193 nm/400 mJ/cm² laser beam, (c) a detail from a pixel of the previous pattern, clearly showing the lift off of AlN in the treated region, (d) a secondary electron image from an AlN:Ag/Si sample that endured the laser treatment (193 nm/300 mJ/cm²).

2. The effect of number of laser pulses: Optical microscopy and XAES spectra

The visual appearance of the treated AlN:Ag will depend on the number of pulses, as expected by the variation of the reflectivity spectra and as confirmed by optical microscopy images shown in Fig.S2a-c. In particular, the samples are , illuminated by (a) white, (b) blue, and (c) red light, while the regions A, B, and C correspond to laser annealing with 2, 1 and no pulse (untreated area), respectively. It is noteworthy that region B is color-sensitive, *i.e.* it can be visually discriminated from the untreated area C when illuminated with blue light (Fig. S2b), but not for the red one (Fig. S2c). The same area can be also visually discriminated when white light is used (Fig. S2a), due to white light containing the spectral range where the LSPR manifests. This observation is quite well understood taking into account the reflectivity enhancement of AlN:Ag at 450 nm after laser annealing with one pulse of 193 nm and the spectrally localized character of the LSPR band. Contrariwise, region A is less color-sensitive and can be easily visually discriminated (even though the reflectivity contrast at red –Fig. S2c- is fainter), in perfect accordance with the enhanced reflectivity of AlN:Ag over almost all the visible spectrum after laser annealing with 2 pulses, possibly due to partial outdiffusion of Ag.

Although the Ag outdiffusion is an undesired side-effect, its study would contribute to the understanding and design of optical encoding processes. In order to quantify the gradual outdiffusion of Ag with the number of pulses, we acquired XAES spectra from the three regions A, B, C of the sample using an $900\ \mu\text{m}^2$ acquisition area, shown in Figs. S2d,e,f. Indeed, there is gradual increase of the peak to peak strength of the Ag_{MNN} XAES signal with the number of pulses at 193 nm and $400\ \text{mJ}/\text{cm}^2$ (Figs. S2d,e,f) providing robust evidence of Ag outdiffusion during laser annealing of AlN:Ag.

The conclusions drawn from the study of the optical reflectivity spectra are supported by optical microscopy images and XAES measurements, similarly to the case of the 193 nm laser. In

particular, Figs. S3a,b,c show the optical microscopy images under white, blue, and red illumination, respectively, from an AlN:Ag sample after laser annealing with 2 (region A) and 5 pulses (region C) of 248 nm; region B is untreated. The untreated area (region C) is darker in accordance with the corresponding reflectivity values. The region C processed with five 248 nm laser pulses under white illumination (Fig. S3a) is bluer in appearance compared to the region A processed with two pulses. This confirms the observed blue-shift in the corresponding reflectivity spectra; the blue-shift after 5 pulses is also confirmed by the bright reflection of region C under blue illumination (Fig. S3b) which is much brighter than the reflection of the same region under red illumination (Fig. S3c).

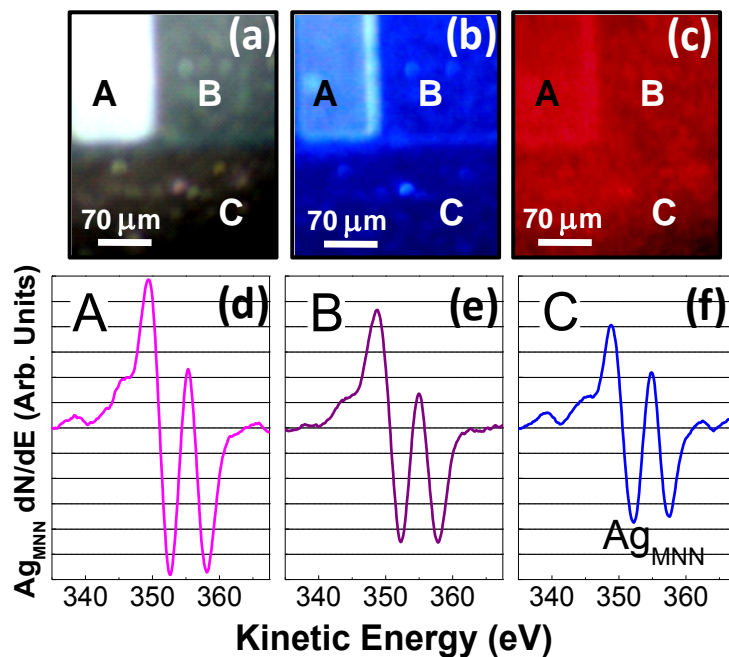


Figure S2: Optical microscopy images of an AlN:Ag sample laser annealed at 193 nm and 400 mJ/cm² under (a) white, (b) blue, and (c) red light illumination. The regions A, B, and C correspond to laser annealing with 2 or 1 pulse and untreated area, respectively. The Auger Ag_{MNN} spectra are also shown for the regions (d) A, (e) B, and (f) C.

XAES spectra from the as grown and laser processed regions (Figs. S3d,e,f) identified a gradual increase of the peak to peak strength of the Ag_{MNN} spectra with the number of 248 nm and 400 mJ/cm^2 laser pulses, providing again robust evidence of Ag outdiffusion during laser annealing of $\text{AlN}:\text{Ag}$; this is also supported by the corresponding topographic XPS image (Fig. S3g) where the counts per second of the emitted $\text{Ag}-3d$ photoelectrons for the regions A,B, and C are recorded.

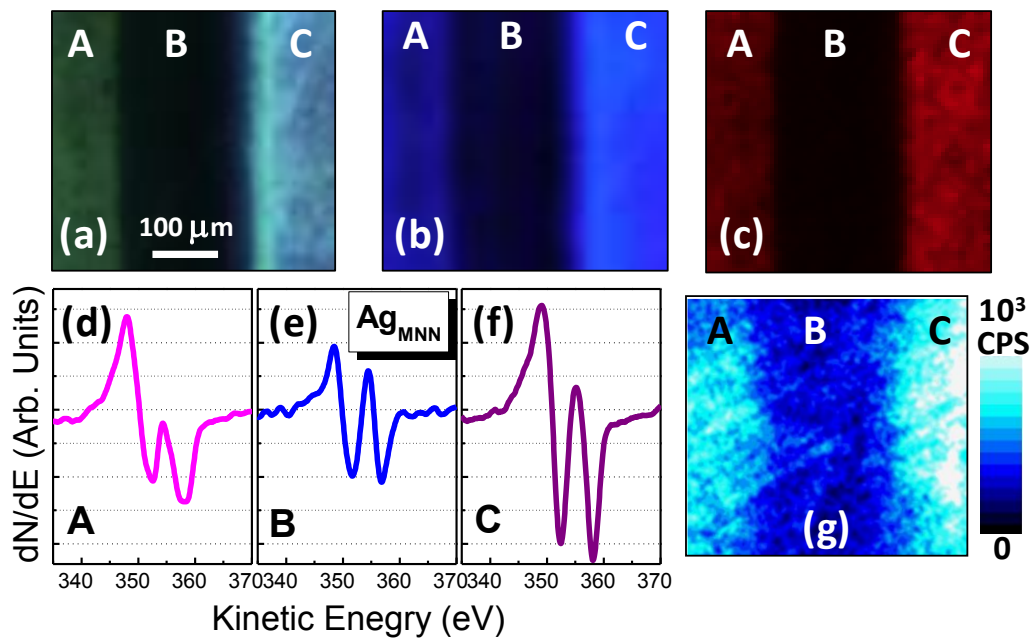


Figure S3: Optical microscopy images under (a) white, (b) blue, and (c) red illumination; XAES spectra of regions (d) A, (e) B, (f) C, respectively, and (g) $\text{Ag}-3d$ imaging XPS, from an $\text{AlN}:\text{Ag}$ sample after laser annealing with 2 (region A) and 5 pulses (region C) of 248 nm; region B is untreated. The same scale bar applies to images (a), (b), (c), and (g).

3. FDTD simulations

The optical reflectance spectra and absorption distribution of the considered nanocomposite AlN:Ag films were studied by Finite Difference Time Domain (FDTD) calculations. FDTD solves the exact 3D full-vector Maxwell's equations on a computational grid, including material dispersion. For the bulk Ag and Si index we perform Drude-Lorentz fits to the corresponding complex dielectric functions (we use data from E.D. Palik). These fits are shown in Fig. S4c-d. To account for small Ag nanoparticles we in addition need to adjust the free-electron relaxation time τ according to $\tau^{-1} \rightarrow \tau^{-1} + v_F / r$, where v_F is the Fermi velocity and r the nanoparticle radius. The index for the AlN matrix in the presence of the Ag nanoparticles is indirectly obtained from ellipsometric measurements of the as-grown samples, by performing a Maxwell-Garnett effective medium fit. The fit yielded a film thickness of 60nm, a Ag nanoparticle size of 3 nm, and a 15% by volume distribution. All these are in excellent agreement with the experimental measurements. The resulting AlN index is shown in Fig. S4b. The measured effective index along with the fitted index for the composite are shown in Fig. S4d.

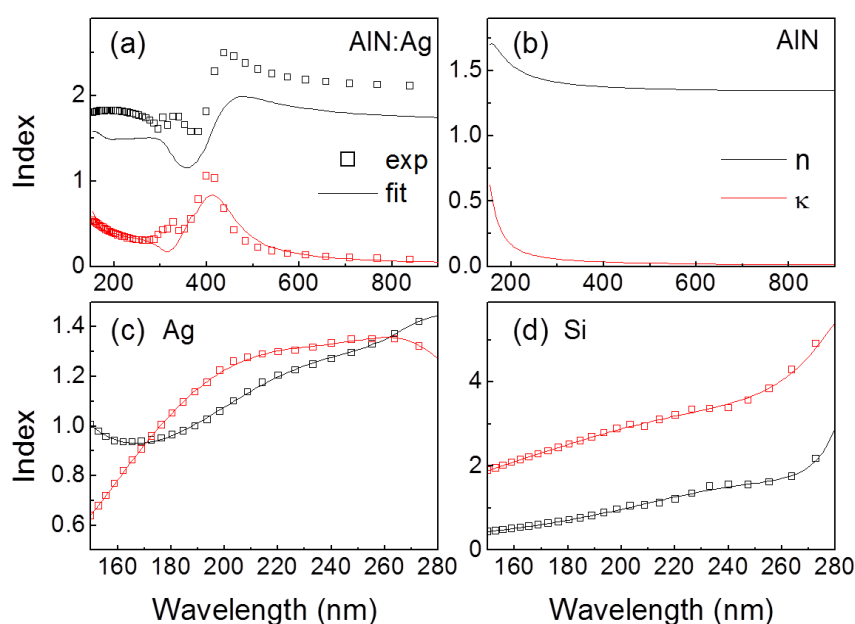


Figure S4: FDTD results.

4. Light absorption in the AlN:Ag/Si system

We study how the size of the Ag nanoparticles affect the absorption distribution within the AlN:Ag film. First, in Fig. S5a we plot the absorption for the random distribution of the 3 nm nanoparticles (solid lines) along with the absorption from an AlN film without the nanoparticles. Evident in all cases are the standing wave patterns created in the 60 nm thick film. Surprisingly, the latter is not significantly less than what we get for the nanostructured case, especially for the 193 nm case. This shows that there is a strong “competition” between matrix and inclusion absorption in the nanostructured film. We stress here that this does not hold a real bulk AlN/Si system. What we examined is a fictitious case: we use the AlN matrix obtained for the AlN:Ag nanostructure in a “bulk” configuration, i.e. without the Ag nanoparticles. We note that experimentally in the absence of nanoparticles the AlN appears much less absorptive -by about an order of magnitude, and thus in reality the bulk AlN absorption is going to be insignificant.

In Fig. S5b-e we examine the effect of different nanoparticle sizes: 3, 6, 10 and 20 nm respectively. To better facilitate our comparison we assume the nanoparticles are ordered in a cubic lattice. This way the regions where we have nanoparticles and the regions where there is clear matrix become evident due to the Ag strong absorption. Remarkably, the nanoparticle size does not seem to significantly modify the overall absorption. Also, in all cases the overall standing wave pattern is well reproduced. In comparing the two different wavelengths, is clear that the 193 nm annealing results into a stronger and better balanced absorption within the nanostructured film. Finally, in Fig. S5f we plot the 20 nm Ag nanoparticle case with a nonabsorbing crystalline ($n=2.1$) AlN shell around it of 2.5 nm thickness. Marginal differences with the corresponding bare Ag nanoparticle case are found.

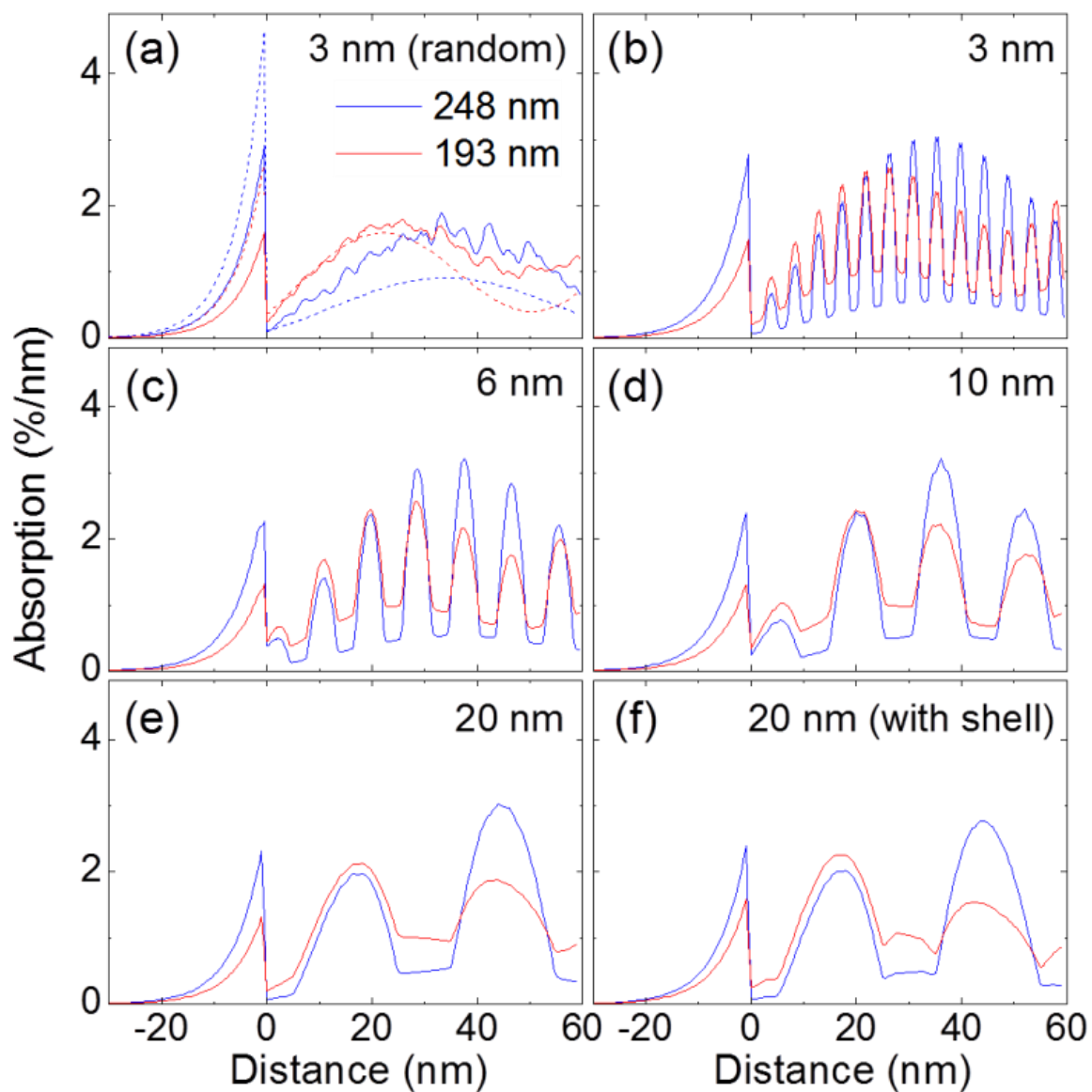


Figure S5: Optical absorption profiles of assemblies of Ag nanoparticles in AlN of size and order (ordered or random).

5. Validity of MG-EMA

Comparison of two different effective medium approximations (EMA). Extraction of effective medium parameters by a full vectorial solution of Maxwell's equations by the FDTD method, and Maxwell-Garnett EMA. In the FDTD approach an exploration of the effects of disorder is possible. Generally all three fairly good agreement. The filling ratio assumed is 11% and the background a dielectric with $n=1.5$ (no absorption). These indicate that in order to get exact fits with the experimental results we should use the FDTD on a disordered case, but this however would be prohibitively expensive computationally. In all our fittings above we used the MG EMA (it is closer to the experimentally-relevant disordered case).

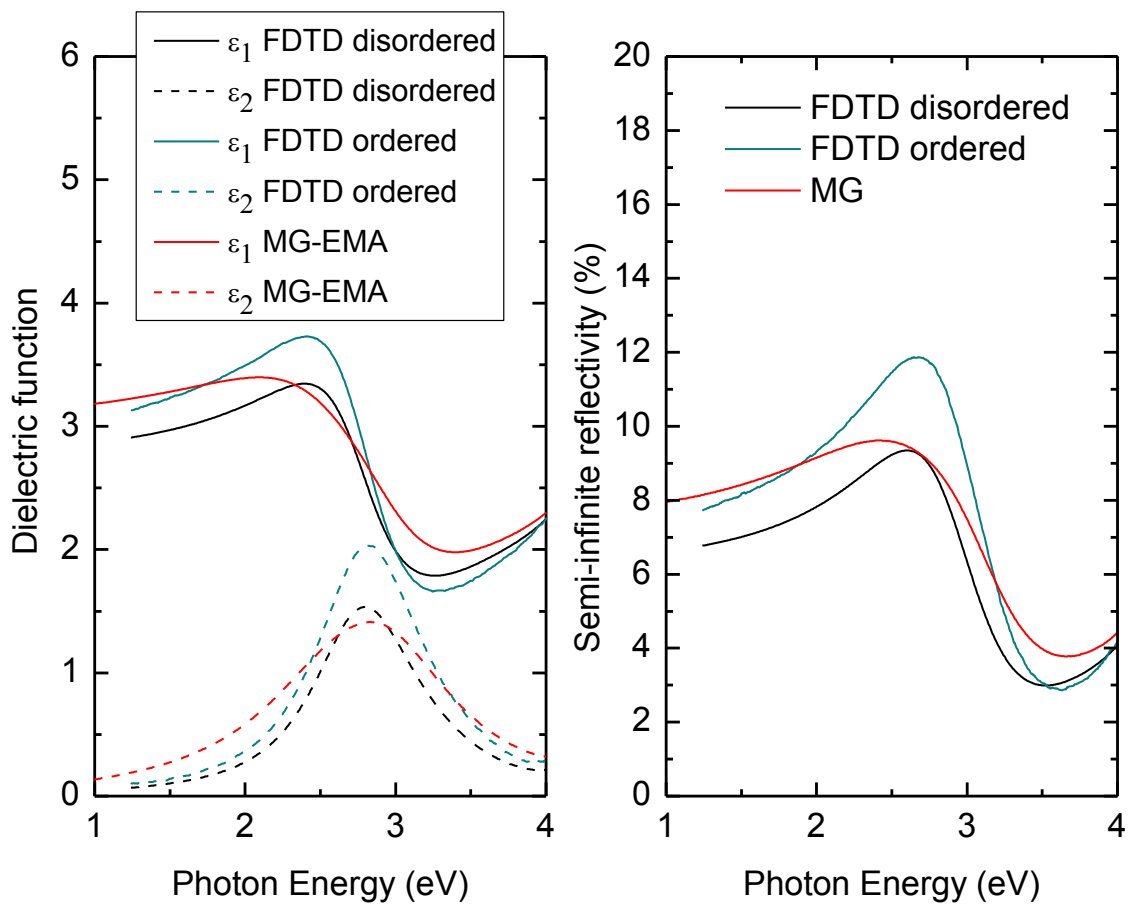


Figure S6: Comparison of MG-EMA results and exact FDTD calculations.

6. Detailed MG-EMA Calculations of the reflectivity of the AlN:Ag/Si system

In order to get insights on the optical effects, which are associated with the experiments and optical encoding presented in the main body of the paper, and to identify the dominant factors that would dictate the spectral reflectivity of the AlN:Ag/Si encoding templates, we performed and present detailed MG-EMA calculations. In particular, we employed extended MG-EMA calculations, which go one step ahead of the ordinary Maxwell-Garnett theory by incorporating characteristics of Mie scattering in the corresponding formulas for the effective dielectric function, as it is described thoroughly by Yanopapas [Phys. Rev. B 75, 035112 (2007)]. The reference dielectric function for the AlN matrix used for the MG-EMA calculations is extracted from the corresponding ellipsometric data presented in Ref. 27 of the main body of the paper. The reference dielectric functions of Ag nanoparticles used in MG-EMA were calculated by considering the dielectric function of bulk Ag [Johnson and Christy, Phys. Rev. B6, 4370 (1972)] and modifying their Drude broadening following the Kreibig's formalism presented in the main body of the paper.

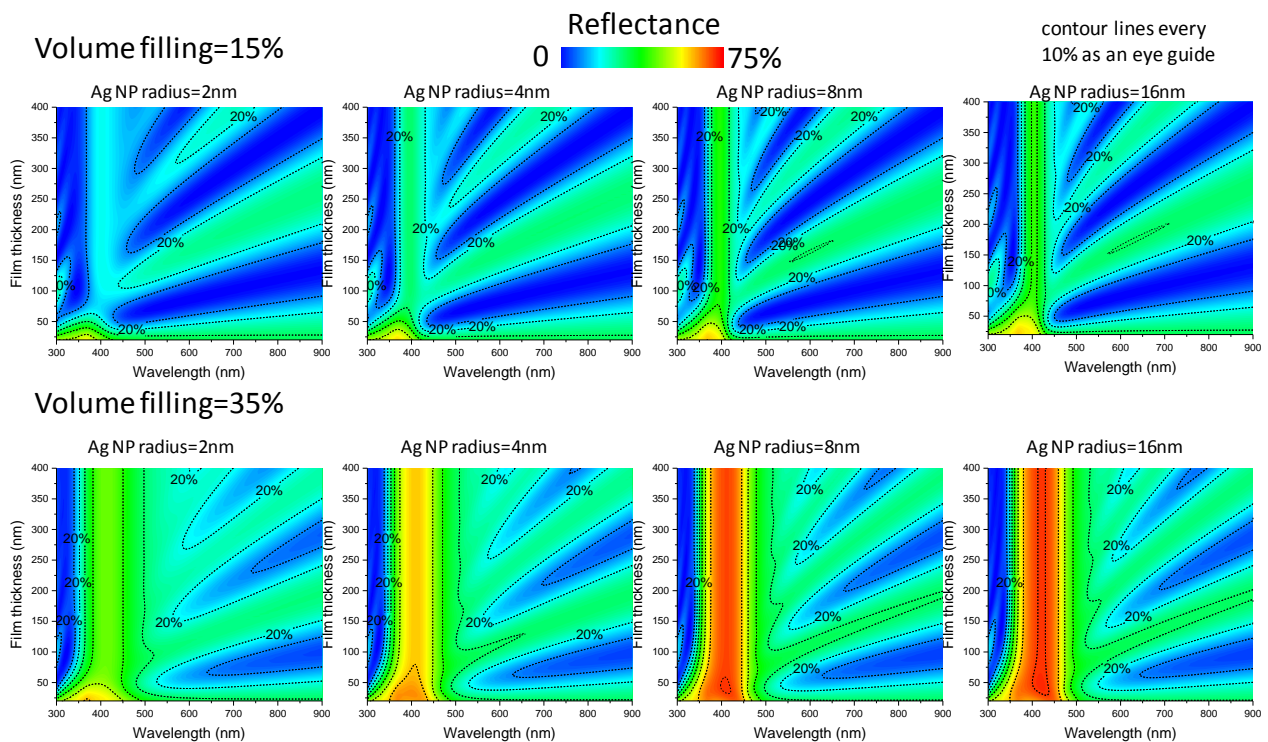


Figure S7: MG-EMA calculations of the reflectivity of AlN:Ag/Si of varying film thicknesses for various Ag particle radii and filling ratios 15% and 35%.

Figure S7 shows extended MG-EMA calculations of the reflectivity of AlN:Ag/Si of varying film thicknesses for various Ag particle radii (2,4,8 and 16 nm) and filling ratios 15% (upper panels) and 35% (lower panels). In all cases, there is a LSPR band around 400 nm whose optical characteristics are quite thickness-independent. On the contrary, thickness-dependent interference fringes manifest for wavelengths longer than 500 nm (presented as blue and green alternating bands).

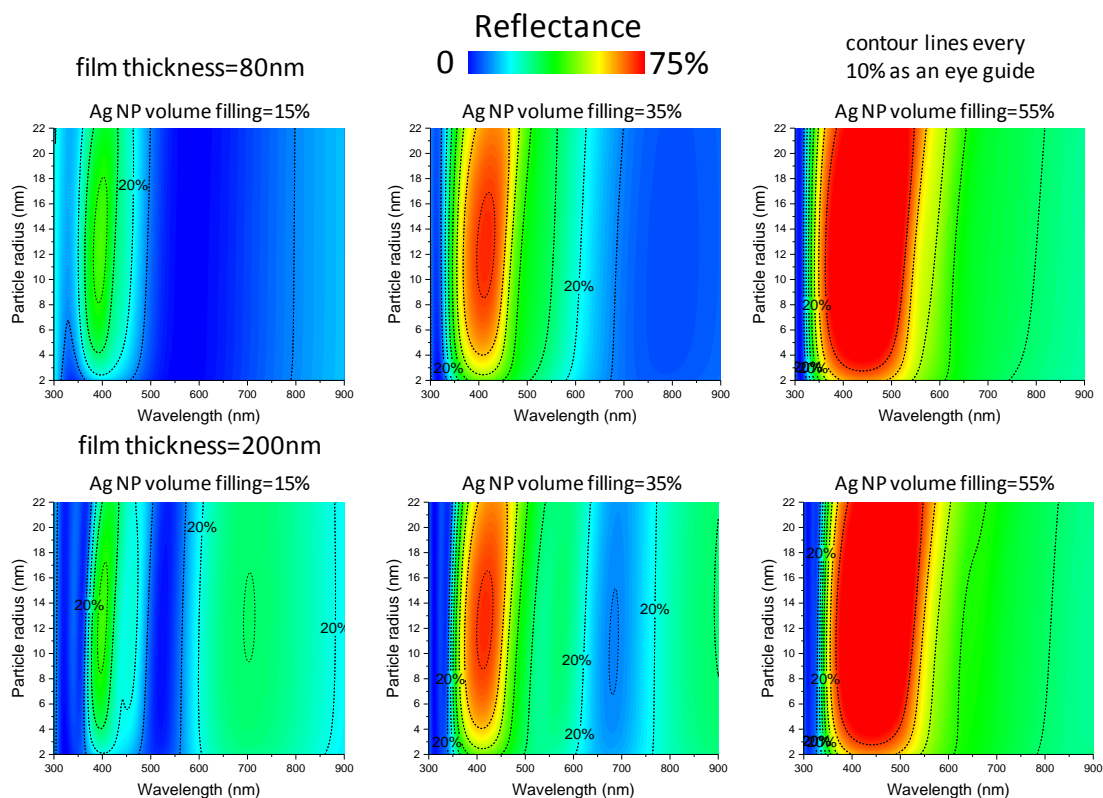


Figure S8: MG-EMA calculations of the reflectivity of AlN:Ag/Si of varying Ag particle radii for various filling ratios and film thickness 80 nm and 200 nm.

Figure S8 shows extended MG-EMA calculations of the reflectivity of AlN:Ag/Si of varying Ag particle sizes for filling ratios (15, 35, and 55 %) and film thickness 80 nm (upper panels) and 200 nm (lower panels). In all cases, there is a LSPR band around 400 nm; this band is slightly shifted to red with increasing Ag particle size. However, this redshift is too weak and cannot explain in its own merit the experimentally observed redshift. Therefore, the matrix change observed for the 193 nm LA by TEM is essential in achieving high reflectivity contrasts between treated and untreated regions AlN:Ag/Si. The increase of filling ratio beyond the 16% (which is similar to our experimental case) broadens and shifts to red the LSPR band. The broadening of the LSPR would

deteriorate the spectral sensitivity of the optical encoding, not to mention that such high filling ratios are not realistic for experimental fabrication, due to percolation of the Ag particles.

7. Durability test of encoded patterns

In order to evaluate the durability of the produced plasmonic patterns we implemented laser annealing with one pulse of 400 mJ/cm^2 of 193 nm and a lithographic mask in order to produce a clearly overt pattern in a AlN:Ag/sapphire template. Then we got white light optical microscopy images of the as patterned sample and after dipping and sonication in acetone, toluene and tetrahydrofuran (THF). Figure S9 shows that the sonication in the organic solvents did not damage the pattern at all. Dipping in HF for a few seconds clearly damaged the pattern, possibly by attacking the underlying sapphire.

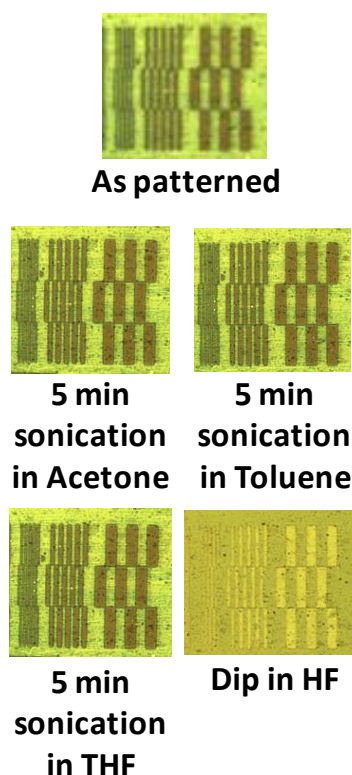


Figure S9: Optical microscopy images of an AlN:Ag plasmonic pattern after dipping to various chemical environments.